Space Weather

RESEARCH ARTICLE
10.1029/2023SW003480

Key Points:

- Validation of ionospheric total electron content (TEC) by the state-of-the-art ionospheric models hosted by NASA Community Coordinated Modeling Center, National Oceanic and Atmospheric Administration Space Weather Prediction Center, and NASA Jet Propulsion Laboratory (JPL)
- Multiple metrics and skill scores are used to assess the performance of ionospheric models in capturing storm time TEC anomaly
- GLObal Total Electron Content and JPL Global Ionospheric Map perform best, and physics-based models perform better than the empirical model in capturing storm TEC variations

Correspondence to:
M.-Y. Chou,
min-yang.chou@nasa.gov

Citation:
Chou, M.-Y., Yue, J., Wang, J., Huba, J. D., El Alaoui, M., Kuznetsova, M. M., et al. (2023). Validation of ionospheric modeled TEC in the equatorial ionosphere during the 2013 March and 2021 November geomagnetic storms. *Space Weather*, *21*, e2023SW003480. https://doi.org/10.1029/2023SW003480

Received 9 MAR 2023
Accepted 17 MAY 2023

Validation of Ionospheric Modeled TEC in the Equatorial Ionosphere During the 2013 March and 2021 November Geomagnetic Storms

Min-Yang Chou[1,2], Jia Yue[1,2], Jack Wang[1,2], J. D. Huba[3], Mostafa El Alaoui[1,2], Maria M. Kuznetsova[1], Lutz Rastätter[1], Ja Soon Shim[4], Tzu-Wei Fang[5], Xing Meng[6], Dominic Fuller-Rowell[5], and John M. Retterer[7]

[1]NASA Goddard Space Flight Center, Community Coordinated Modeling Center, Greenbelt, MD, USA, [2]Department of Physics, Catholic University of America, Washington, DC, USA, [3]Syntek Technologies, Fairfax, VA, USA, [4]Department of Atmospheric Sciences, Yonsei University, Seoul, South Korea, [5]NOAA Space Weather Prediction Center, Boulder, CO, USA, [6]Jet Propulsion Laboratory, California Institute of Technology, Pasadena, CA, USA, [7]Institute for Scientific Research, Boston College, Chestnut Hill, MA, USA

Abstract This paper presents the validation of modeled total electron content (TEC) from 14 ionospheric models, including empirical, physics-based, and data assimilation (DA) models, hosted by the NASA/NSF Community Coordinated Modeling Center (CCMC), NOAA Space Weather Prediction Center, and NASA Jet Propulsion Laboratory (JPL). This study aims to assess the current progress and capability of the CCMC-hosted ionospheric models in capturing the storm time ionosphere during the low and moderate solar flux years. We focus on the low-latitude ionosphere (i.e., ±40° in magnetic latitude) and compare the modeled TEC with the Madrigal TEC during the 2013 March and 2021 November storms. Multiple metrics are used to quantitatively assess the models' accuracy, precision, association, bias, and capability in capturing the TEC changes in response to the storms. The skill score based on the metric scores is further proposed to evaluate the overall performance of ionospheric models against the reference model (International Reference Ionosphere 2016; IRI-2016). The results indicate that the DA model GLObal Total Electron Content and JPL Global Ionospheric Map models show good performance in modeling the TEC and reasonably reflect the storm time TEC changes spatially and temporally. The empirical models IRI-2016 and 2020 show relatively good performance compared with the physics-based models regarding the model-data comparison; however, it is difficult to characterize the TEC changes caused by storms. The physics-based models can simulate the storm effect in spatial and temporal TEC variations better than the empirical model. The performance of ionospheric models in capturing the storm time TEC anomaly is presented and discussed.

Plain Language Summary The Earth's ionosphere is highly variable due to atmospheric variations and solar activity. Forecasting the ionosphere is of particular importance because the ionosphere significantly impacts our daily lives. Scientists have developed multiple numerical models, such as empirical, physics-based, data-assimilation, and machine learning models, to improve our capability in capturing space weather and understanding the underlying physics responsible for ionospheric variability. NASA Goddard Space Flight Center Community Coordinated Modeling Center (CCMC) hosts an extensive suite of state-of-the-art ionospheric models, providing the community access to these modern models to support space weather and space physics research. CCMC also acts as an unbiased evaluator to validate models for eventual use in space weather forecasting. This paper aims to validate the performance of recently onboarded CCMC, National Oceanic and Atmospheric Administration Space Weather Prediction Center, and NASA Jet Propulsion Laboratory ionospheric models during the geomagnetic storms, providing a baseline for users and modelers to understand the recent progress of ionosphere models.

1. Introduction

Over the past decades, the rapid development of a wide range of ionospheric models, such as empirical models (Bilitza et al., 2017, 2022; Goncharenko et al., 2021), physics-based models (e.g., Huba & Liu, 2020; McDonald et al., 2015; Richmond et al., 1992; Ridley et al., 2006; Schunk et al., 2002), data assimilation (DA) models (e.g., Chartier et al., 2021; Chen et al., 2016; Hsu et al., 2018; C. Y. Lin et al., 2017; Schunk et al., 2004; Sun et al., 2017), and machine learning models (e.g., L. Liu et al., 2022), has facilitated our understanding of the

complex physical coupling processes of the magnetosphere/ionosphere/thermosphere/lower atmosphere system. The ultimate goal of these models is to better understand the near-Earth space environment, mitigating the impacts of space weather on our daily life (e.g., Fang et al., 2022; Kataoka et al., 2022; Shultz, 2014). Of particular significance is to forecast the ionospheric space weather because the ionosphere significantly impacts satellite and radio communication (Basu et al., 2001). Since the ionosphere is affected by the energy and momentum that originate from the neutral atmosphere and magnetosphere/solar wind, accurately modeling of the ionosphere is challenging and of operational importance for the space weather forecast.

A systematic and quantitative evaluation of space weather models is an essential part of model development processes to verify the validity and pinpoint the missing underlying physics, as well as to advance the models' capability for the space weather forecast (e.g., Cai et al., 2022; Chen et al., 2016; Fuller-Rowell et al., 2000; C.-Y. Lin et al., 2020; D. Lin et al., 2022; H.-L. Liu et al., 2018; Perlongo et al., 2018; Retterer, 2005; Scherliess et al., 2006). NASA Goddard Space Flight Center Community Coordinated Modeling Center (CCMC) is a multi-agency partnership aimed at the research to support the dissemination and development of advanced space science and space weather models. The CCMC hosts a large suite of state-of-the-art ionospheric models developed by the broad space weather and aeronomy community, providing the community access to these modern models to support space weather and space physics research. Additionally, CCMC acts as an unbiased evaluator to provide a mechanism by which research and/or operational models can be validated, tested, and improved for eventual use in space weather forecasting. To support community-wide modeling validation projects, CCMC initiated the Coupling, Energetic, and Dynamics of Atmospheric Regions (CEDAR) electrodynamic thermosphere ionosphere challenge in 2009 and CEDAR-Geospace Environment Modeling (GEM) modeling challenge in 2011. The CEDAR and CEDAR-GEM modeling challenges paid great attention to evaluating the modeled parameters, including ionospheric F layer peak electron density (NmF2), peak density height (hmF2), vertical ion drift, Joule heating, neutral density, and total electron content (TEC), during both quiet and storm times (Rastätter et al., 2016; Shim et al., 2011, 2012). In 2018, CCMC established an *International Forum for Space Weather Modeling Capabilities Assessment* to assess the predictive capabilities of space weather models (Scherliess et al., 2019; Shim et al., 2018). Besides the validation projects, CCMC also developed the Comprehensive Assessment of Models and Events Using Library Tools (CAMEL) and Kamodo frameworks to support the community for model-data comparison (Rastätter et al., 2019; Ringuette et al., 2022).

Recently, several state-of-the-art ionospheric models, including Sami3 is also a model of the ionosphere (SAMI3 v3.22), Thermosphere Ionosphere Electrodynamics General Circulation Model (TIEGCM v2.0), SAMI3-TIEGCM, Whole Atmosphere Community Climate Model with thermosphere and ionosphere extension (WACCM-X), Physics Based MODel (PBMOD) and International Reference Ionosphere (IRI-2020), have been installed at NASA CCMC for the run-on-request and instant run (https://ccmc.gsfc.nasa.gov/tools/runs-on-request/). CCMC partners with the National Oceanic and Atmospheric Administration Space Weather Prediction Center (NOAA SWPC) and NASA Jet Propulsion Laboratory (JPL) to evaluate the performance of ionospheric models. Therefore, the goal of this paper is to present the preliminary validation results of current CCMC-hosted ionospheric models, NOAA SWPC GLObal Total Electron Content (GloTEC), the coupled Whole Atmosphere Model-Ionosphere Plasmasphere Electrodynamics (WAM-IPE), and NASA JPL Global Ionospheric Map (GIM). Two geomagnetic storms during the 2013 March and 2021 December are selected to assess the models' performance in moderate and low solar flux years. The modeled TEC is compared with the ground-based GNSS TEC observations from the Madrigal TEC. Four categories of metrics are utilized for model-data comparison, including accuracy, bias, association, and precision. In addition to model-data comparison, we evaluate the models' capability in capturing the TEC changes in response to the storms. More detailed investigation on the impacts of model parameter settings to reproduce the storm effects is beyond the scope and should be carried out individually for each model. This study focuses on the overall performance of equatorial ionospheric TEC during storm times.

2. Models and Observations

2.1. Ground-Based GNSS TEC Observation

The ground-based GNSS vertical TEC maps developed by the Massachusetts Institute of Technology Haystack Observatory (Madrigal TEC) are used to evaluate the performance of ionospheric models during storm times. The Madrigal TEC has spatial and temporal resolutions of $1° \times 1° \times 5$ min. Due to the discrepancy of spatial

resolution and cadence between the model outputs and Madrigal TEC observations, TEC maps derived from the ionospheric models are interpolated into $1° \times 1° \times 1$ hr and only compare the locations where TEC observations are available on an hourly basis. Note that this study focuses on the equatorial ionization anomaly (EIA) region; only the Madrigal TEC observations within $\pm 40°$ magnetic latitudes are used for validation.

2.2. Empirical and Data-Assimilation Models

The ionospheric models used for validation include empirical, physics-based, data-assimilation models, and NASA JPL GIM. The empirical models used in this study are IRI-2016 (Bilitza et al., 2017) and IRI-2020 (Bilitza et al., 2022). IRI is an international project sponsored by the Committee on Space Research and the International Union of Radio Science (URSI). The major data sources are the worldwide network of ionosondes, incoherent scatter radars, the ISIS and Alouette topside sounders, and in-situ measurements from satellites and rockets. The IRI outputs are generated based on the standard setting of the model. IRI-2020 includes more satellite measurements and an equatorial vertical ion drift model (Fejer et al., 2008). IRI-2016 and 2020 are currently available for instant run and run-on-request at CCMC (https://kauai.ccmc.gsfc.nasa.gov/instantrun/iri). A detailed description of the major update of IRI-2020 is given in Bilitza et al. (2022). The spatial and temporal resolutions of IRI TEC outputs used in this study are $5° \times 5° \times 1$ hr.

NASA JPL GIM is like a data-driven or DA model in that the global TEC maps are generated by incorporating the ground-based GNSS TEC measurements and climatological models (Mannucci et al., 1998, 1999). This approach is based on interpolating TEC within triangular tiles combined with the polynomial fitting that tessellates the ionosphere modeled as a thin spherical shell. TEC over the ocean regions is provided from the Bent climatological ionosphere model (Bent et al., 1975; Llewellyn & Bent, 1973) to fill the gap, and the Kalman filter is further applied for smoothing the maps in time. JPL GIM provides TEC maps with the spatial and temporal resolution of $1° \times 1° \times 15$ min.

The data-assimilation models are NOAA SWPC GloTEC and WAM-IPE. GloTEC is an empirical model-based DA scheme used to optimally estimate the three-dimensional ionospheric electron density. This model uses a Gauss-Markov Kalman filter and IRI-2016 as a background ionospheric model. It can assimilate the ground-based GNSS TEC observations from hundreds of dual-frequency ground-based GNSS receivers worldwide and RO slant TEC observations from the FORMOSAT-7/COSMIC2 mission, providing near real-time global TEC maps, peak density (NmF2), peak density height (hmF2), and TEC anomaly. GloTEC being analyzed in this study is the version with only ground-based GNSS data, which has been in operation since late 2019. GloTEC provides TEC maps with the spatial and temporal resolution of $1° \times 1° \times 15$ min.

WAM-IPE is a physics-based whole atmosphere DA model that specifies ionosphere and thermosphere conditions in response to solar, geomagnetic, and lower atmospheric forcing (e.g., Fang et al., 2022). WAM is a general circulation model for the neutral atmosphere extending from the ground to the top of the thermosphere (~600 km depending on the solar activity, e.g., Fuller-Rowell et al., 2008). The WAM state is updated using the 3DVar DA technique in the lowest 60 km of the atmosphere using a modified version of the Gridpoint Statistical Interpolation software. An Incremental Analysis Update method is used to apply the increment across the assimilation window to prevent the damping of tidal waves from the DA process. IPE is a time-dependent and global three-dimensional ionosphere-plasmasphere-electrodynamics model extending from 90 km to approximately 10,000 km (e.g., Maruyama et al., 2016). All neutral atmosphere fields from WAM have been one-way coupled to IPE to enable the plasma to respond to changes driven by the neutral atmosphere. Weimer empirical model and TIROS auroral empirical models driven by the solar wind data are used to specify the external energy input from the magnetosphere. It should be mentioned that the 2021 model output used in this study is the operational version, which has been available since 2021, but the 2013 model output is free run without DA. WAM-IPE provides TEC maps with the spatial and temporal resolution of $4° \times 2° \times 10$ min in longitude, latitude, and time.

2.3. Physics-Based Models

The physics-based models include SAMI3 v3.22, TIEGCM v2.0, Coupled Thermosphere Ionosphere Plasmasphere Electrodynamics model (CTIPe), Global Ionosphere Thermosphere Model (GITM), WACCM-X, and PBMOD. The physics-based and empirical models mentioned above are available through the run-on-request at NASA CCMC. More detailed information on CCMC ionospheric models is given at https://ccmc.gsfc.nasa.gov/models/.

Three versions of SAMI3 are performed for the validation. The first version is SAMI3 v3.22, which uses the neutral compositions, temperatures, and neutral winds derived from empirical NRLMSIS2.0 and Horizontal Wind Model 14 (HWM14), as well as high-latitude electric fields calculated from the empirical Weimer model (Weimer, 2005) for the potential. The second version is SAMI3-Rice Convection Model (RCM) (Huba & Sazykin, 2014; Huba, Sazykin, & Coster, 2017). The coupled SAMI3-RCM is used to simulate the ionosphere-plasmasphere-ring current response to geomagnetic storms. The RCM provides high-latitude field-aligned currents, which can generate penetration electric fields to the low- to mid-latitude ionosphere (Huba et al., 2005; Kelley et al., 2003). SAMI3-RCM is currently unavailable for run-on-request at CCMC but will be likely available in the future. The third version is SAMI3-TIEGCM, which is similar to the default SAMI3 v3.22, but the neutral compositions, temperatures, and winds are specified by TIEGCM (e.g., Chen et al., 2013; Huba, Maute, & Crowley, 2017), with more variability than NRLMSIS2.0 and HWM14. The SAMI3 v3.22 and SAMI3-TIEGCM TEC maps have spatial and temporal resolution of ~3.75° × 1.8° × 15 min in longitude, latitude and time. SAMI3-RCM has the spatial and temporal resolution of ~2.5° × 1.8° × 15 min in longitude, latitude, and time.

The NCAR TIE-GCM is a comprehensive, first-principles, three-dimensional, non-linear representation of the coupled thermosphere and ionosphere system that includes a self-consistent solution of the low-latitude electric field. The model solves the three-dimensional momentum, energy, and continuity equations for neutral and ion species at each time step, using a semi-implicit, fourth order, centered finite difference scheme, on each pressure surface in a staggered vertical grid. TIEGCM parameterizes energetic particle precipitation in the high latitude and polar region (Roble & Ridley, 1987). The polar region energy inputs associated with electric potential and auroral particle precipitation are prescribed either by empirical Weimer or Heelis (Heelis et al., 1982) models and analytical auroral model (Roble & Ridley, 1987). At the lower boundary, atmospheric tides are specified using the Global Scale Wave Model. In this study, the standard TIEGCM v2.0 is used for validation (https://ccmc.gsfc.nasa.gov/models/TIE-GCM~2.0), and both TIEGCM v2.0 with high latitude electric potential inputs from Weimer and Heelis empirical models are performed. For more details about TIEGCM v2.0 is given at https://www.hao.ucar.edu/modeling/tgcm/. The TIEGCM TEC maps have the spatial and temporal resolution of 2.5° × 2.5° × 20 min.

CTIPe model is a nonlinear, coupled thermosphere-ionosphere-plasmasphere electrodynamic model that consists of four components: a global thermosphere, a high-latitude ionosphere, a mid- and low-latitude ionosphere/plasmasphere, and an electrodynamical calculation of the global dynamo electric field. The magnetospheric input to the model is based on the statistical models of auroral precipitation and electric fields described by Fuller-Rowell and Evans (1987) and the empirical Weimer model. The thermosphere model was developed by Fuller-Rowell and Rees (1980). The thermosphere model simulates the time-dependence of the wind vector, temperature, and neutral density by numerically solving the nonlinear primitive equations of momentum, energy, and continuity. A detailed description of CTIPe is given by Codrescu et al. (2012). In this study, CTIPe v4.1 is used for validation (https://ccmc.gsfc.nasa.gov/models/CTIPe~4.1). CTIPe provides TEC maps with the spatial and temporal resolution of 18° × 2° × 15 min in longitude, latitude, and time.

The GITM-SWMF simulations are provided by the University of Michigan. GITM is a 3-dimensional spherical code that models the Earth's thermosphere and ionosphere (Ridley et al., 2006). In this study, the high-latitude inputs of electric field and precipitation are from the two-way coupled Block-Adaptive-Tree-Solar wind-Roe-Upwind-Scheme (BATSRUS) and RCM within the Space Weather Modeling Framework (SWMF, Tóth et al., 2005, 2012). The coupled model is driven by the actual solar wind data from OMNIweb. MSIS (e.g., Hedin, 1991) and IRI (Bilitza, 2001) are used to set the initial state. A detailed description of GITM-SWMF is given by Wang et al. (2019). GITM-SWMF provides TEC maps with the spatial and temporal resolution of 4° × 1° × 30 min in longitude, latitude and time.

WACCM-X is a configuration of the NCAR Community Earth System Model (CESM, Hurrell et al., 2013) that extends the atmospheric component into the thermosphere with the upper boundary between 500 and 700 km. Physical processes represented in WACCM-X build upon those in regular WACCM and the Community Atmosphere Model, which has a model top at ~130 and ~40 km, respectively. In this study, WACCM-X v2.2 (e.g., H.-L. Liu et al., 2018) is used for validation (https://ccmc.gsfc.nasa.gov/models/WACCMX~2.2). The current CCMC WACCM-X can use Weimer or Heelis empirical model for specifying the high-latitude electric potential. Auroral particle precipitation is specified by an analytical auroral model (Roble & Ridley, 1987). In this study, the Heelis empirical model is used to drive the WACCM-X. WACCM-X provides TEC maps with the spatial and temporal resolution of 1.25° × 0.94° × 10 min in longitude, latitude, and time.

The PBMOD ionospheric model (Retterer, 2005) is a system of Physics Based MODels that describes the three-dimensional time-dependent evolution of the low-latitude ionosphere (±40° in latitude) on several different spatial scales: it provides the global plasma density and composition at altitudes between 90 and 2,000 km; at finer scales it describes the development of fluid plasma turbulence within this region and the resulting radio scintillation. PBMOD uses neutral wind, temperature, and compositions derived from the climatological HWM07 (Drob et al., 2008) and MSIS models. Plasma temperatures in the low-latitude region are modeled by the Titheridge plasma temperature model (Titheridge, 1997). The plasma drift is specified using the Scherliess-Fejer model (Scherliess & Fejer, 1999). Detailed information on PBMOD is given at https://ccmc.gsfc.nasa.gov/models/PBMOD~1/. PBMOD provides TEC maps with the spatial and temporal resolution of 10° × 1° × 15 min in longitude, latitude, and time.

3. Metrics and Skill Score

To assess and quantify the ionospheric model performance, four categories of metrics, including accuracy, bias, association, and precision, are utilized to address specific aspects of the model-data relationship (Liemohn et al., 2021). The accuracy metric used in this study is root mean square error (RMSE): $\mathrm{RMSE} = \sqrt{\frac{1}{N}\sum_{i=1}^{N}(M_i - O_i)^2}$, where M and O denote the model and observational values, respectively. RMSE quantifies the overall difference and quality of the model-data comparison. The bias metric is the mean error (ME): $\mathrm{ME} = \overline{M} - \overline{O}$. A negative ME indicates a systematic underestimation of the model values, while a positive ME indicates a systematic overestimation of the model values. The association metric is the Pearson linear correlation coefficient (R): $R = \frac{\sum_{i}^{N}\left(O_i - \overline{O}\right)\left(M_i - \overline{M}\right)}{\sqrt{\sum_{i}^{N}\left(O_i - \overline{O}\right)^2 \sum_{i}^{N}\left(M_i - \overline{M}\right)^2}}$, which measures the strength of the linear relationship between the model and observation. The precision metric is the difference in standard deviations between the model and observation ($P_{\sigma,\mathrm{diff}}$): $P_{\sigma,\mathrm{diff}} = \sigma_M - \sigma_O$. $P_{\sigma,\mathrm{diff}}$ with a value above or below zero indicates that the model over or under predict the spread of the data.

Next, we calculate the skill score (SS) for comparing the metric values (RMSE, ME, R, $P_{\sigma,\mathrm{diff}}$) against a reference model. The SS is defined as: $\mathrm{SS} = \frac{\mathrm{Metric\_new} - \mathrm{Metric\_ref}}{\mathrm{Metric\_perfect} - \mathrm{Metric\_ref}}$. Metric_ref represents the metric values of a reference model, which can be any model. Here IRI-2016 is set as a reference model. Metric_new represents the metric values of a new model. Metric_perfect is the best metric value for data-model comparison. The SS is, therefore, equal to one if the new model is perfect. If SS = 0, this indicates that the performance of the new model is the same as the reference model. A negative SS denotes a worse skill than the reference model. We further normalize each metric's SS ($n\mathrm{SS} = \frac{\mathrm{SS} - \mathrm{SS\_min}}{\mathrm{SS\_max} - \mathrm{SS\_min}}$) for calculating the total nSS ($\sum n\mathrm{SS}$). SS_max and SS_min denote the maximum and minimum SS among the models. The maximum and minimum of total nSS are equal to four (four metrics) and zero. The performance of the physics-based, empirical, and data-assimilation models during storms can be evaluated and compared.

Considering that the metrics mentioned above mainly focus on the difference between models and observations, they cannot well assess the models' capability in capturing the ionospheric storm anomaly. Thus, we further estimate the relative TEC change (TC) between the quiet and storm time: $\mathrm{TC} = \frac{\mathrm{TEC_{storm}} - \mathrm{TEC_{quiet}}}{\mathrm{TEC_{quiet}}} \times 100\%$. $\mathrm{TEC_{quiet}}$ is the period before the storm, and $\mathrm{TEC_{storm}}$ is the period during the main and recovery phases of the storm (see Figure 1). The quantities of TC reveal the ionospheric responses to the geomagnetic storms. The metrics based on the ratio of TC are used to assess the model's capability in capturing the storm-induced TEC changes during the main and recovery phases (i.e., Shim et al., 2012, 2018). The first metric is the ratio of model and observation TC difference between the 80th and 20th percentiles ($\mathrm{ratio(80th\,percentile - 20th\,percentile)} = \frac{(\mathrm{TC}_M)_{80\mathrm{th}} - (\mathrm{TC}_M)_{20\mathrm{th}}}{(\mathrm{TC}_O)_{80\mathrm{th}} - (\mathrm{TC}_O)_{20\mathrm{th}}}$), and the other one is the ratio of model and observation TC at the 80th percentile ($\mathrm{ratio(80th\,percentile)} = \frac{(\mathrm{TC}_M)_{80\mathrm{th}}}{(\mathrm{TC}_O)_{80\mathrm{th}}}$). $(\mathrm{TC}_M)_{80\mathrm{th}}$ and $(\mathrm{TC}_O)_{80\mathrm{th}}$ are the TC of models and observations at 80th percentile during the main and recovery phases of geomagnetic storms. Shim et al. (2018) calculated the ratios using the maximum and minimum TC values. Here we choose the 80th and 20th percentiles to avoid outliers. The correlation coefficient between TC_M and TC_O is also calculated to assess the model's capability in capturing the spatial distribution of ionospheric anomaly.

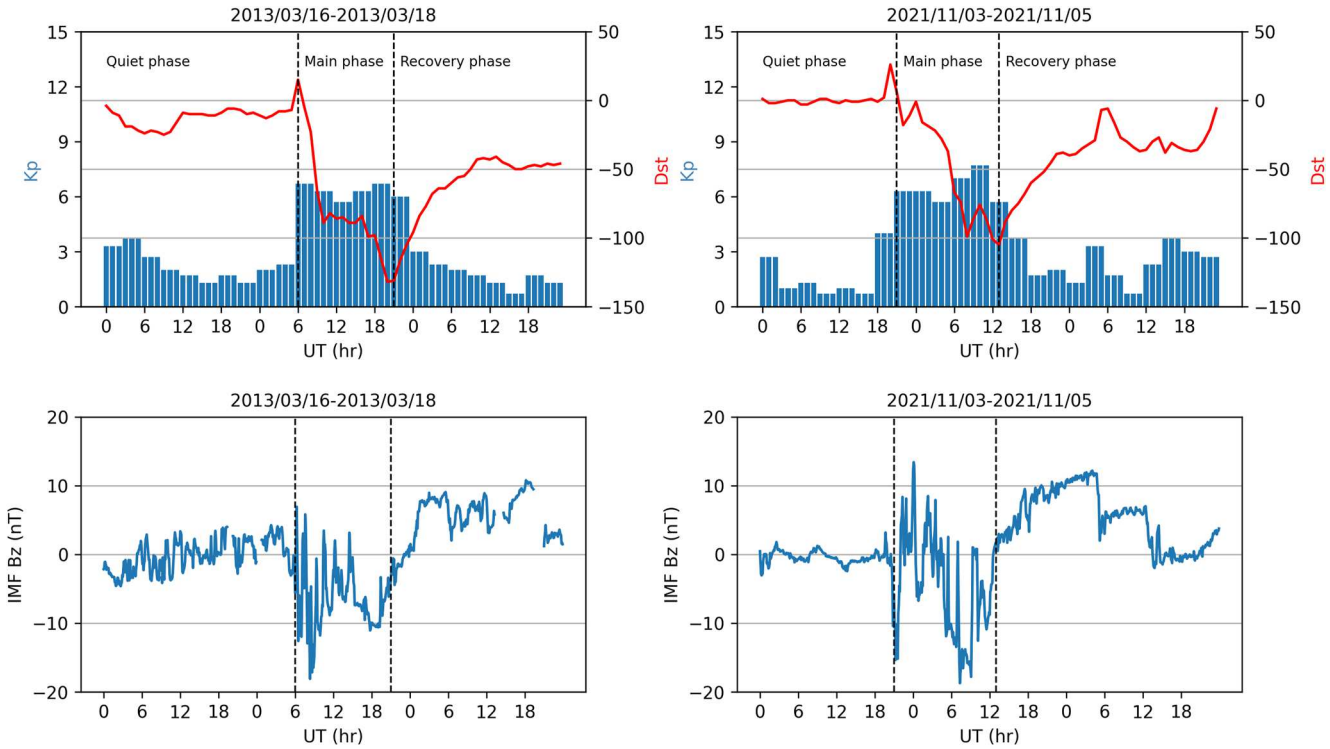

Figure 1. Dst, Kp, and Interplanetary magnetic field Bz values for the 2013 March and 2021 November storm events.

4. Results

Two coronal mass ejections driven geomagnetic storms during 16–18 March 2013 and 3–5 November 2021 are selected to evaluate the performance of ionospheric models in TEC during the storm times in the moderate and low solar flux years. Figure 1 shows the Dst, Kp, and Interplanetary magnetic field (IMF) Bz index for the 2013 March (left panels) and 2021 November (right panels) storms. Both storms have peak Dst values of −124 and −105 and are considered to be moderate to strong geomagnetic storms with Kp ranging from 6 to 7. The durations of quiet time, main phase, and recovery phase of the storms indicated by black dashed lines are defined based on the Dst and Kp values. The bottom panels of Figure 1 show that the corresponding IMF Bz for the 2013 March and 2021 November storms turn southward with intermittent fluctuations as the Dst index decreases during the main phases, and gradually turn northward during the recovery phases. Both storms have similar peak IMF Bz values of −18.09 and −18.72 during the main phases. In this study, we focus on the EIA region (i.e., ±40° magnetic latitudes) and the ionospheric model TEC during the quiet time, main, and recovery phases of the storms are evaluated, respectively.

4.1. 2013 March Storm

Figure 2 shows the TEC maps as a function of local time (LT) and magnetic latitude (MLAT) for each model during the quiet time (pre-storm phase), main phase, and recovery phase of the 2013 March storm. These TEC maps are constructed by binning the TEC data into 0.5 hr × 0.5° (LT × MLAT) grids and taking the average values in each grid point. A Gaussian filter with a standard deviation of 1.5 for the 2D Gaussian kernel is then applied to smooth the TEC maps. The madrigal TEC shows clear TEC enhancements (decreases) in the daytime (nighttime) during the main phase of the storm compared with the quiet time TEC. The EIA structure extends to higher latitudes during the main phase and shrinks to lower latitudes during the recovery phase. It is suggested to be related to the enhancement of daytime eastward electric field by superposed penetration electric fields when the IMF Bz turns southward during the main phase of the storm (Figure 1); stronger EIA can develop with significant TEC enhancement (e.g., Rajesh et al., 2021).

Similar storm effects can also be identified in GloTEC, JPL GIM, SAMI3-RCM, WAM-IPE, WACCM-X, TIEGCM-Weimer, TIEGCM-Heelis, CTIPe, and PBMOD. We note that the empirical model IRI-2016 and

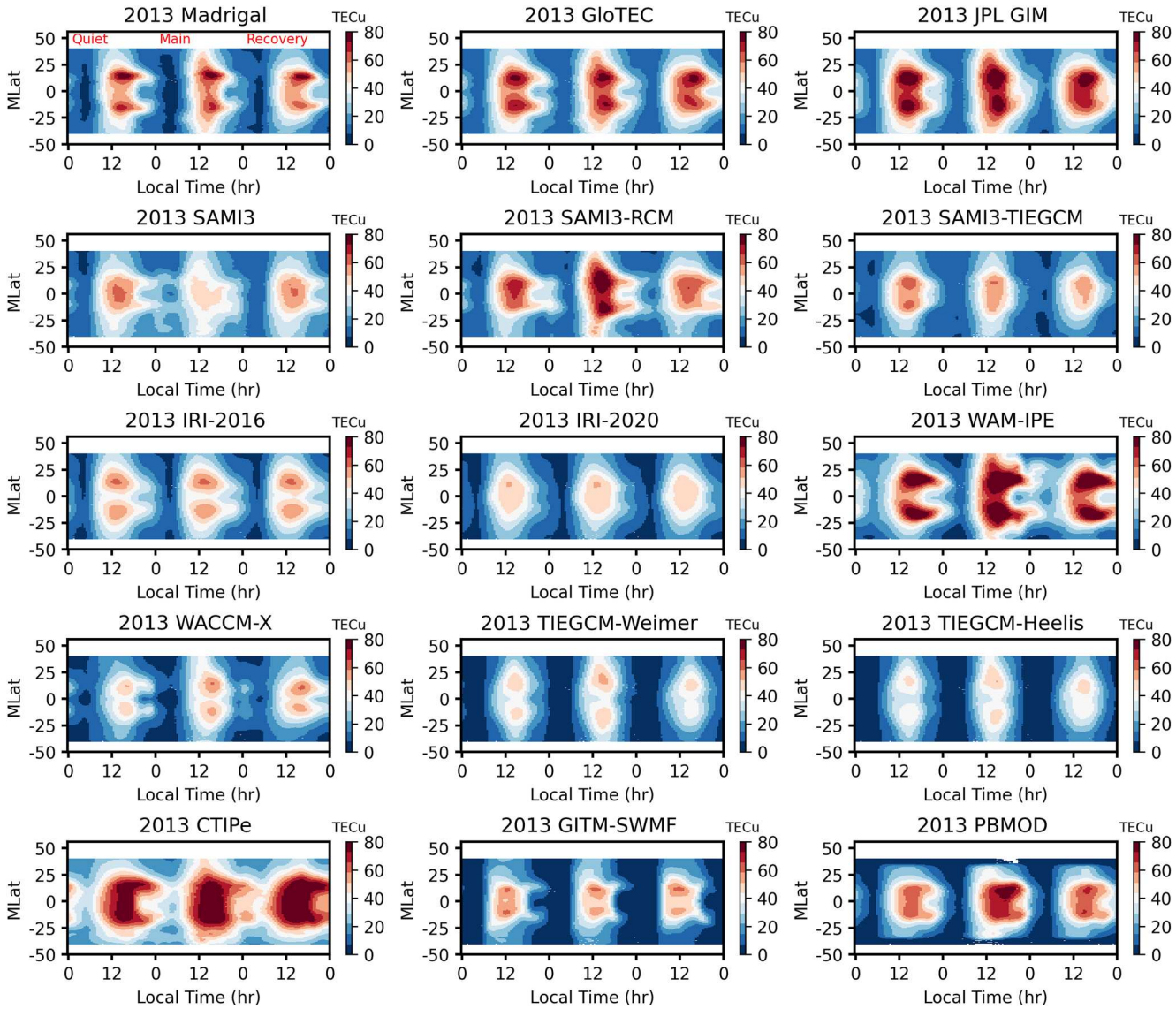

Figure 2. Total electron content (TEC) maps as a function of local time and magnetic latitudes for the madrigal TEC and all modeled TEC during the quiet time, main, and recovery phases of the 2013 March storm.

2020 do not capture the storm effect and tend to be smaller than the observations. The physics-based models SAMI3, SAMI3-TIEGCM, WACCM-X, TIEGCM-Weimer, TIEGCM-Heelis, GITM-SWMF, and PBMOD tend to underestimate the TEC in the EIA region, and WAM-IPE and CTIPe overestimate the TEC. The underestimation of TEC for WACCM-X, TIEGCM-Weimer, TIEGCM-Heelis and GITM-SWMF could be partly due to the upper boundary being limited to ~600 km. Overall, the DA model GloTEC, JPL GIM, and physics-based model SAMI3-RCM show the EIA structures similar to Madrigal TEC, despite the TEC values being systematically larger than the Madrigal TEC.

To quantitatively evaluate the accuracy, precision, association, and bias of ionospheric models, Figure 3 shows the RMSE, $P_{\sigma,\mathrm{diff}}$, R, and ME for each model during the quiet time, main and recovery phases of the 2013 March storm. In the accuracy category, the statistical results indicate that the DA model GloTEC has the smallest RMSE of ~7.66–7.7 TECu among the three phases compared with empirical and physics-based models. The RMSE tends to increase during the main phase of the storm for most models except WACCM-X and TIEGCM-Heelis. The RMSE then decreases during the recovery phase of the storm except for WAM-IPE, TIEGCM-Weimer/Heelis, and CTIPe. The empirical model IRI-2016 shows a smaller RMSE of ~9 TECu than other physics-based models

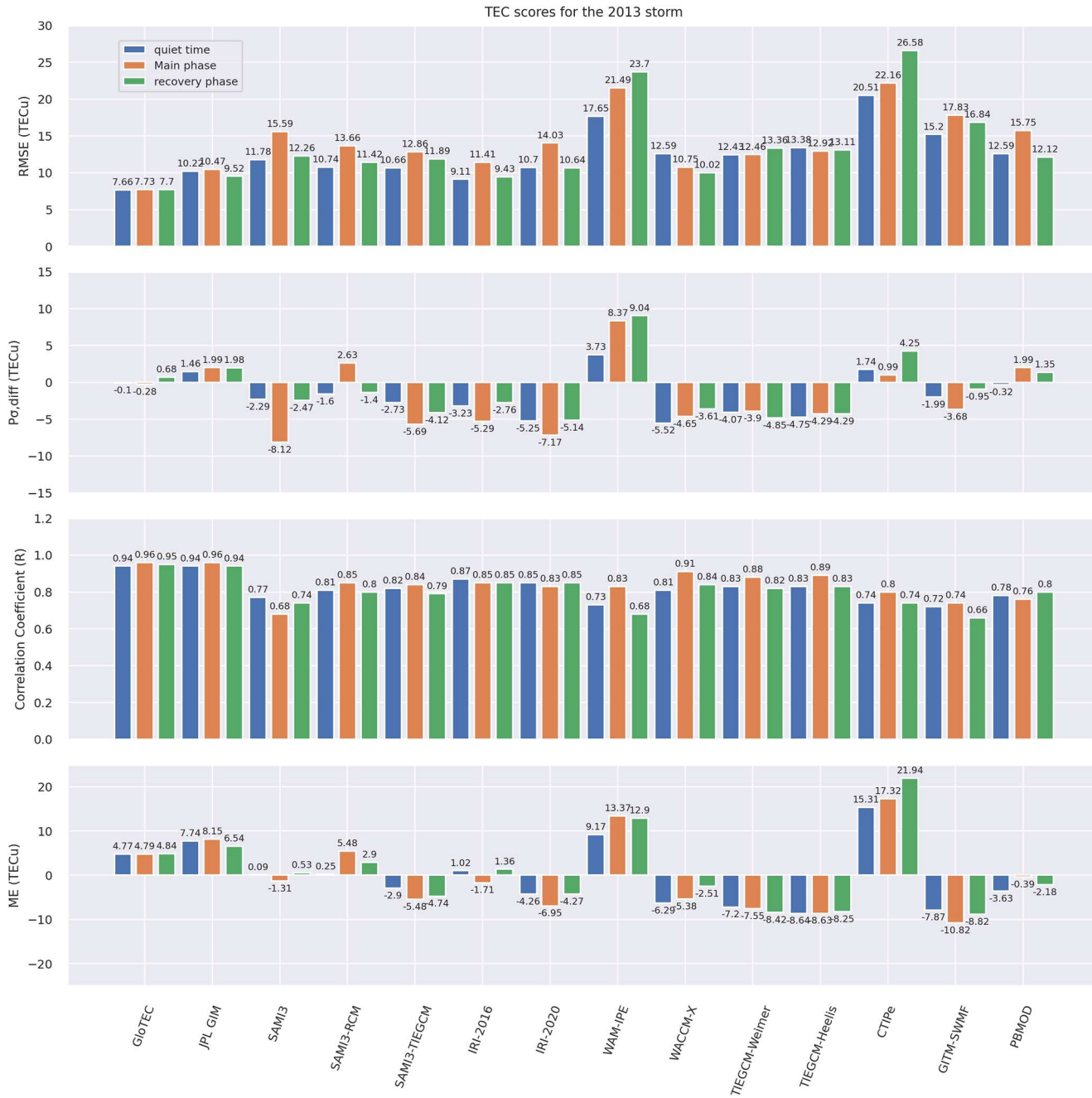

Figure 3. Histograms of root mean square error, $P_{\sigma,\mathrm{diff}}$, Correlation Coefficient, and mean error for all ionospheric models during the quiet time (blue bars), main (orange bars), and recovery phases (green bars) of the 2013 March Storm.

during the quiet time and recovery phase, but RMSE increases to 11.41 TECu during the main phases. The overall accuracy of IRI-2016 is better than IRI-2020. For the physics-based models, WACCM-X has a smaller RMSE of ∼10–12 TECu during the main and recovery phases compared with other physics-based models. SAMI3-RCM and SAMI3-TIEGCM tend to have smaller RMSE than SAMI3 by ∼1–2 TECu. The WAM-IPE and CTIPe have greater RMSE over 17 TECu than other models.

In the precision ($P_{\sigma,\mathrm{diff}}$) category, the GloTEC shows high precision, with the smallest $P_{\sigma,\mathrm{diff}}$ ranging from −0.28 to 0.68 TECu among all ionospheric models, demonstrating that GloTEC well captures the spread of ionospheric TEC. JPL GIM has $P_{\sigma,\mathrm{diff}}$ about 1.5–2 TECu. Most physics-based and empirical models tend to underestimate the spread of TEC by 1.5–8 TECu, except WAM-IPE and CTIPe overestimate the spread of TEC. WAM-IPE

significantly overestimates the spread of TEC by 8–9 TECu during the storm times, and SAMI3 significantly underestimates the spread of TEC by ∼8 TECu during the main phase. PBMOD shows better precision of −0.32 to 1.99 TECu compared with another physics-based model. CTIPe has the highest precision of 0.99 TECu among other physics-based and empirical models during the main phase.

In the association category, GloTEC and JPL GIM have higher correlation coefficients (R) of ∼0.94–0.96 during the three phases. The empirical model IRI-2016 and 2020 also have R ranging from 0.83 to 0.87, and IRI-2016 performs slightly better than IRI-2020. For the physics-based model, WACCM-X shows the highest R of 0.91 and 0.84 during the main and recovery phases. Overall, most models have R above 0.8. SAMI3, WAM-IPE, CTIPe, and GITM-SWMF tend to have lower R (<0.8).

In the model bias category, GloTEC, JPL GIM, SAMI3-RCM, WAM-IPE, and CTIPe systematically overestimate the TEC, and SAMI3-TIEGCM, IRI-2020, WACCM-X, TIEGCM-Weimer/Heelis, GITM-SWMF, and PBMOD systematically underestimate the TEC. SAMI3 and IRI-2016 have smaller biases ranging from −1.31 to 0.53 and −1.71 to 1.36 TECu, respectively. GloTEC has a bias of ∼4.8 TECu, and JPL GIM has biases ranging from ∼6.5 to 8 TECu. WAM-IPE and CTIPe systematically overestimate the TEC by 9–13 and 15–22 TECu, respectively. The other physics-based models tend to have bias ranging from −11 to −3 TECu.

Figure 4 shows the heatmaps of the normalized skill scores (top panel) for each model to compare the performance of ionospheric models against the reference model IRI-2016 during three phases. The normalized skill scores are calculated based on the metric scores shown in Figure 3. The maximum and minimum normalized skill scores are equal to 1 and 0. The bottom panel shows the total normalized skill scores, which is the summation of normalized skill scores from the accuracy, precision, association, and bias categories. Note that the normalized skill scores are calculated independently during the three phases. The total normalized skill scores reveal that GloTEC, JPL GIM, and IRI-2016 are the top three ionospheric models based on those fit performance metrics. Among the physics-based model, SAMI3-RCM, WACCM-X, and PBMOD have better performance compared with other physics-based models. Although WACCM-X shows degradation during the quiet time, the overall performance during the storm times is better than other physics-based models.

However, the total normalized SS reveals that the fit performance metrics cannot well assess the models' capability in modeling the storm effect. It is apparent that the empirical model IRI-2016 does not show significant ionospheric responses to the storm (Figure 2), but the metric scores are higher than other physics-based models. This could be because the physics-based models often systematically underestimate or overestimate the TEC, resulting in significant errors when conducting model-data comparisons. However, the physics-based models are more able to predict the TEC changes. To assess the models' capability in response to the storm effect, we calculate the relative TEC change between the quiet and storm times ($\mathrm{TC} = \frac{\mathrm{TEC_{storm}} - \mathrm{TEC_{quiet}}}{\mathrm{TEC_{quiet}}} \times 100\%$).

Figure 5 shows the TC maps as a function of LT and MLAT during the main and recovery phases of the storm. The Madrigal TEC shows zonal average TEC variations of about ±25% during the main and recovery phases, displaying a fork-shape distribution of TEC enhancements. The GloTEC and JPL GIM show similar ionospheric variations of about ±25% and fork-shape patterns comparable with the Madrigal TEC, demonstrating that both models can capture the storm effects. The empirical model IRI-2016 and 2020 do not show apparent TEC variations during the storm times. For the physics-based models, all the models show clear TEC variations during the storm time, implying that the physics-based models are more suitable for the storm study. These physics-based models show clear TEC enhancements in the equatorial ionosphere, although the amplitude and TEC variations are not totally consistent with the Madrigal TEC. We note that SAMI3 and SAMI3-RCM significantly overestimate the midnight TEC during the storm times, but SAMI3-TIEGCM shows some improvements. This implies that the empirical MSISNRL00 and HWM14 models used in SAMI3 and SAMI3-RCM do not represent the actual situation.

To quantify the models' capability in capturing the TEC variations during the storm times, Figure 6 shows the ratios and correlation coefficient of TC. The line plot and histogram in the top panel of Figure 6 denote the ratio of the TC difference from the 80th to 20th percentiles between models and observation ($\mathrm{ratio(80th-20th)} = \frac{(\mathrm{TC}_M)_{80\mathrm{th}} - (\mathrm{TC}_M)_{20\mathrm{th}}}{(\mathrm{TC})_{80\mathrm{th}} - (\mathrm{TC}_O)_{20\mathrm{th}}}$) and the TC difference from the 80th to 20th percentiles ($(\mathrm{TC})_{80\mathrm{th}} - (\mathrm{TC})_{20\mathrm{th}}$). The histogram shows that Madrigal TEC has TC of ∼49%–51% during the main and

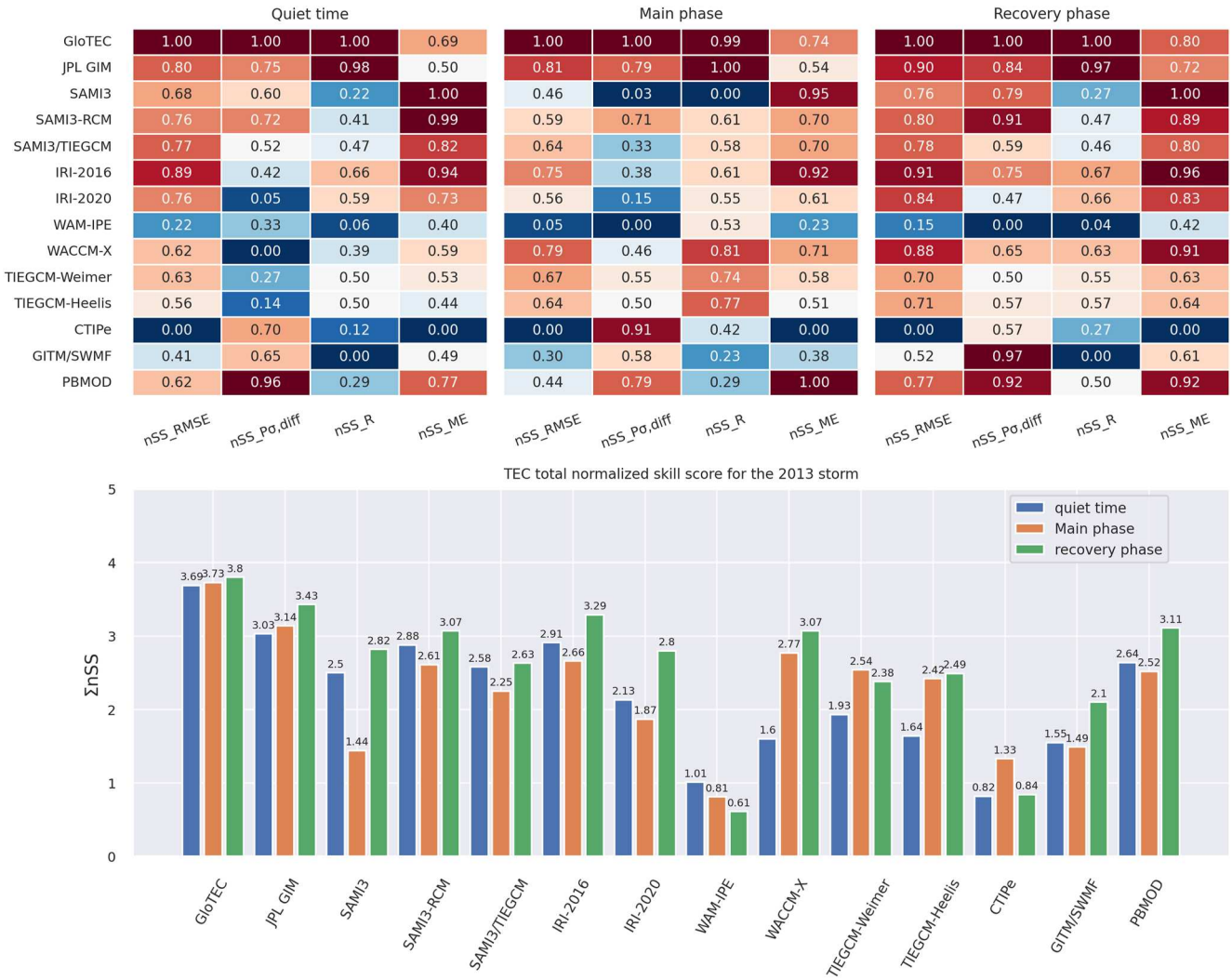

Figure 4. (top) The normalized skill score of root mean square error, $P_{\sigma,\mathrm{diff}}$, R, and mean error for each model during the quiet time (left), main phase (middle), and recovery phase (right) of the 2013 March storm. (bottom) The summation of normalized skill scores for each model.

recovery phases, generally consistent with Figure 5. The line plot shows that GloTEC and JPL GIM have ratios of 0.73 and 0.74, demonstrating that both models slightly underestimate the TC difference. GloTEC and JPL GIM have TC ranging from ~36% to 40%. The IRI models fail to simulate the storm effects with ratios close to 0 and TC of ~6%–10%. The physics-based model TIEGCM-Weimer shows the best performance with ratios close to 1 and TC of ~51%–52%. SAMI3-RCM also has ratios of 1.15 and 0.9, but TC values are slightly larger (~57%) and smaller (~46%) than Madrigal TEC during the main and recovery phases. CTIPe has ratios of 0.78 and 0.68, and TC differences of ~35%–39%.

Next, we evaluate the models' capability to predict the positive TEC changes due to the storm. The line plot and histogram in the middle panel of Figure 6 are the ratios of TC at the 80th percentile and TC at the 80th percentile for each model. Madrigal TEC shows that the storm mainly causes about 28% and 22% positive TEC variations during the main and recovery phases. The GloTEC and JPL GIM show ~21% positive TEC variations during the main phase, and ~14% and 11% during the recovery phase. Both models slightly underestimate the positive TEC changes. IRI 2016 and 2020 models only have ~1%–2% positive TEC changes, and the TC(80th) ratios are close to 0. For the physics-based models, SAMI3, TIEGCM-Weimer, TIEGCM-Heelis, CTIPe, and GITM-SWMF have ratios close to 1 and TC(80th) of ~25%, 28%, 31%, 34%, and 22%, respectively, during the main phase; however, degradation occurred during the recovery phase.

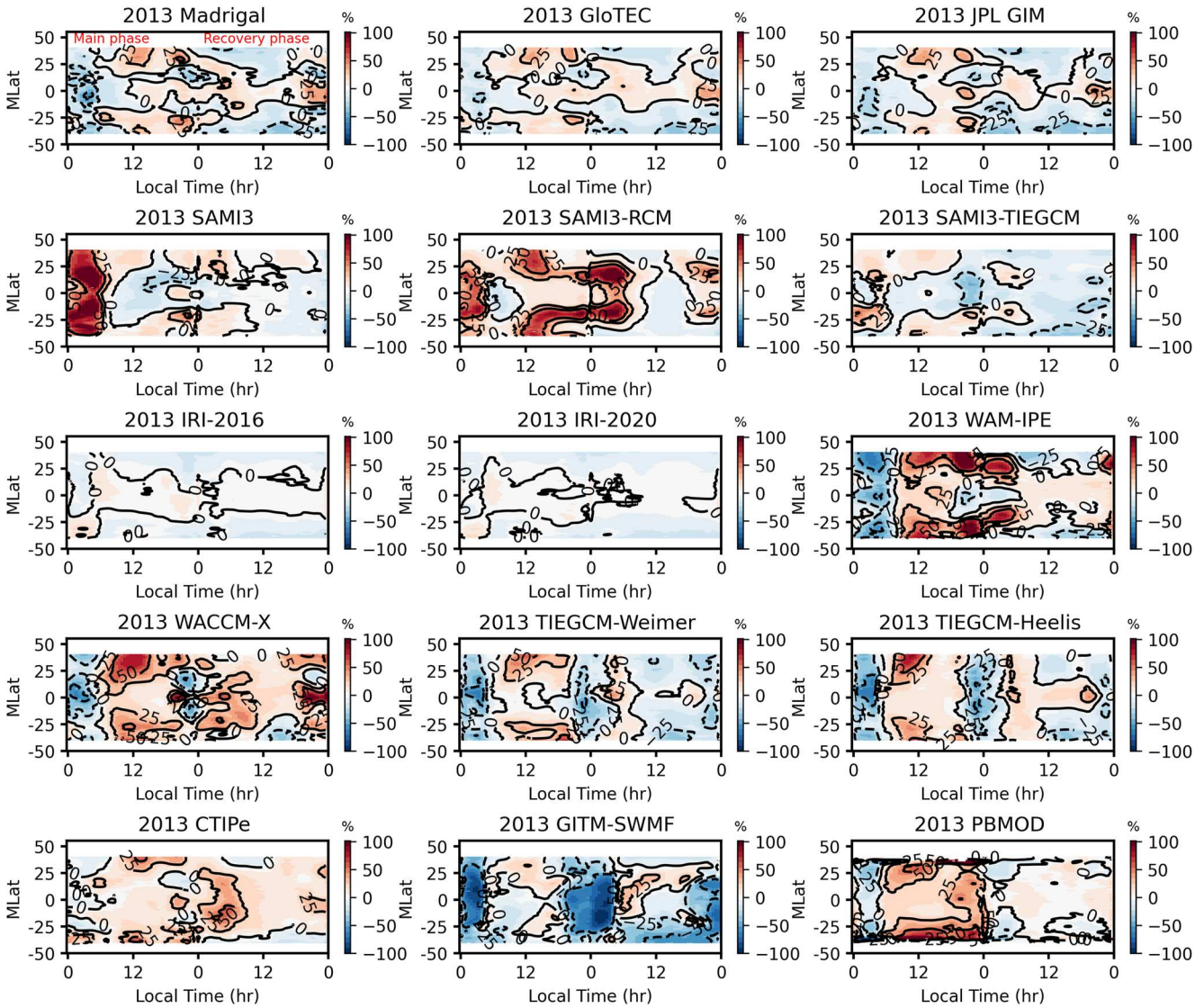

Figure 5. The total electron content (TEC) change maps as a function of local time and magnetic latitudes for the Madrigal TEC and ionospheric models during the main and recovery phases of the 2013 March storm.

The bottom panel shows the correlation coefficient of TC. The GloTEC and JPL GIM show higher correlation coefficients of 0.55–0.64. For the physics-based models, CTIPe has the highest correlation coefficient of ~0.33 during the main and recovery phases. Note WACCM-X also shows relatively higher correlation coefficients of ~0.21–0.22 during the main and recovery phases, suggesting that the spatial and temporal distribution of TEC changes are reasonable compared with Madrigal TEC (Figure 5), although the TEC changes are significantly overestimated.

Overall, GloTEC and JPL GIM show good performance in capturing the storm effect. TIEGCM-Weimer can reasonably simulate the TEC relative changes during the main phase of the storm than other physics-based and empirical models. However, the performance degrades during the recovery phase. CTIPe shows TEC relative changes close to Madrigal TEC and the highest correlation coefficient of 0.33, despite CTIPe systematically overestimating the TEC (Figure 2).

Figure 6. The ratios and correlation coefficient of total electron content change (TC). (top) The line plot and histogram denote the ratio of the TC difference from the 80th to 20th percentiles between models and observation (ratio(80th − 20th) = $\frac{(\mathrm{TC}_M)_{80\mathrm{th}} - (\mathrm{TC}_M)_{20\mathrm{th}}}{(\mathrm{TC}_O)_{80\mathrm{th}} - (\mathrm{TC}_O)_{20\mathrm{th}}}$) and the TC difference from the 80th to 20th percentiles ($((\mathrm{TC})_{80\mathrm{th}} - (\mathrm{TC})_{20\mathrm{th}}$). (middle) The ratios of TC at the 80th percentile and TC at the 80th percentile for each model. (bottom) Correlation coefficients of TC.

4.2. 2021 November Storm

Figure 7 is the same as Figure 2 but for the 2021 November storm. The Madrigal TEC also shows clear TEC enhancements (decreases) in the daytime (nighttime) during the main phase of the storm. The EIA extends to higher latitudes during the main phase and shrinks to lower latitudes during the recovery phase. The difference between the 2013 March and 2021 November storms is that the TEC during the recovery phase is greater than the TEC during the main phase, which could be partly due to the spatial distribution of daytime Madrigal TEC observations. On the other hand, in the periods of intermittent northward turning of IMF Bz during the main phase of the storm (Figure 1), the penetration of magnetospheric overshielding electric field might cause a westward perturbation (Kelley et al., 1979), thus inhibiting the daytime upward $E \times B$ drift and mitigating the TEC enhancement.

The TEC enhancements due to the storm can be identified from most models, despite the existence of systematic bias. The GloTEC and JPL GIM have EIA structures identical to the Madrigal TEC during three phases; however, their TEC values are overestimated. Note that the empirical model IRI-2016 and 2020 also show TEC enhancements during the storm time, which is different from the 2013 March storm. It should be mentioned that TIEGCM-Weimer/Heelis significantly underestimated the TEC by a factor of ∼7. A similar underestimation of TEC also appears in SAMI3/TIEGCM.

Figure 8 shows the RMSE, $P_{\sigma,\mathrm{diff}}$, R, and ME for each model during the quiet, main, and recovery phases of the 2021 November storm. In the accuracy category, the RMSE tends to increase during the main and recovery

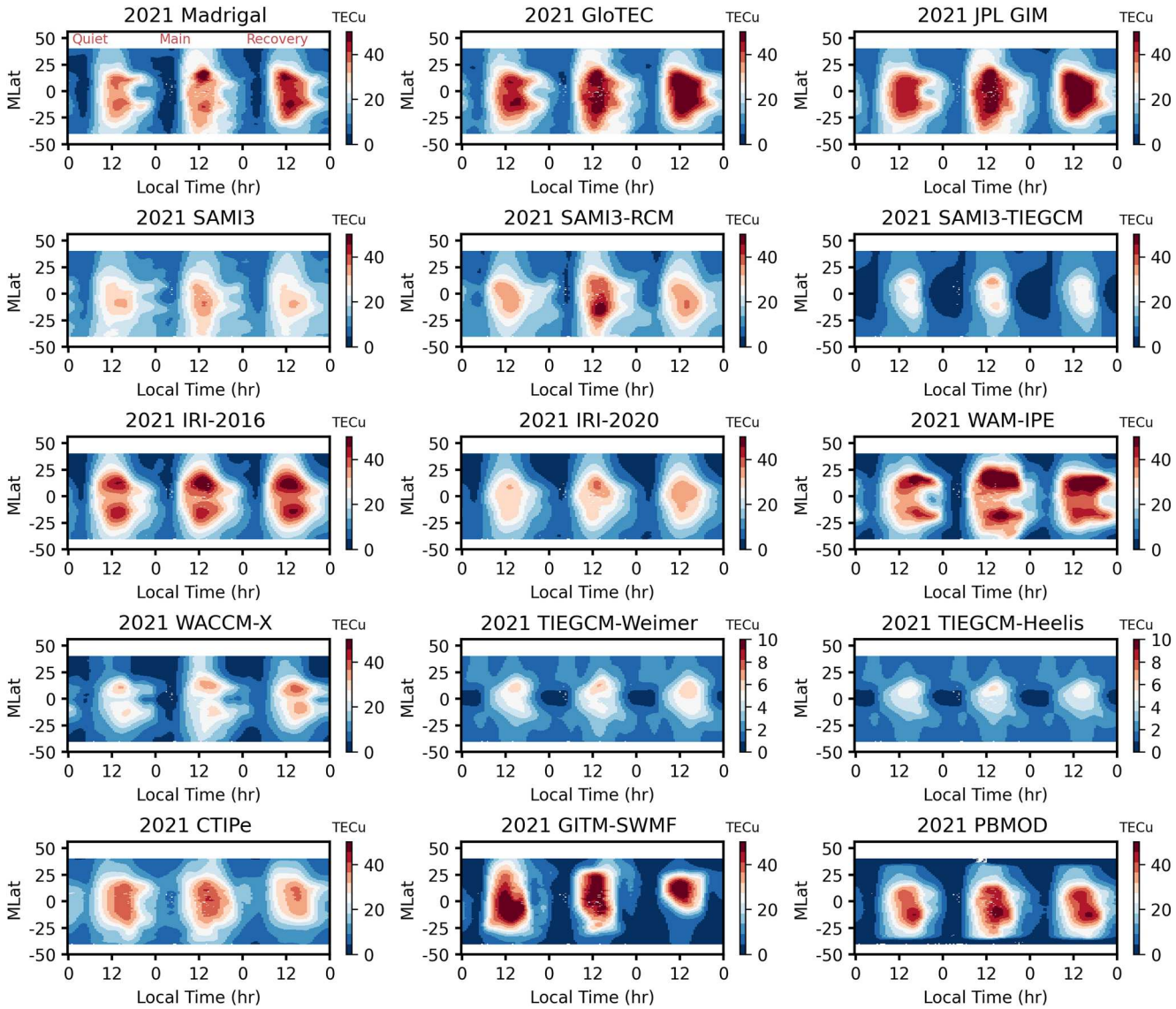

Figure 7. Same as Figure 2 but for the 2021 November storm.

phases of the storm for all the ionospheric models. The statistical results show that the DA model GloTEC and JPL GIM have similar and smallest RMSE ranging from 5 to 6 TECu. The empirical model IRI-2016 and 2020 have RMSE ranging from 5 to 7.6 TECu, slightly larger than GloTEC and JPL GIM. For the physics-based models, SAMI3-RCM has the smallest RMSE of 5.74–7.93 TECu. WACCM-X, CTIPe, and PBmod also show similar RMSE ranging from 6.94 to 9.44 TECu. TIEGCM-Weimer/Heelis have the largest RMSE ranging from ∼16 to 20 TECu due to the underestimation of TEC (Figure 7).

In the precision ($P_{\sigma,\mathrm{diff}}$) category, the PBMOD shows the highest precision with the smallest $P_{\sigma,\mathrm{diff}}$ of 0.56, −0.68, and −0.08 TECu during the three phases. GloTEC and JPL GIM have similar $P_{\sigma,\mathrm{diff}}$ ranging from 0.79 to 1.42 TECu. For the empirical models, IRI-2016 has higher precision of about −0.86 to 1.21 TECu. We find SAMI3, SAMI3-RCM, SAMI3-TIEGCM, IRI-2020, WACCM-X, TIEGCM-Weimer/Heelis, and GITM-SWMF tend to underestimate the spread of TEC by 2–13 TECu, and WAM-IPE and CTIPe overestimate the spread of TEC by 1.5–6 TECu.

In the association category, GloTEC and JPL GIM again have similar and highest correlation coefficients (R) of ∼0.93–0.95 during the three phases. The empirical model IRI-2016 and 2020 have R ranging from 0.83 to 0.9, and IRI-2020 performs slightly better than IRI-2016 during the storm times. For the physics-based model, SAMI3-RCM, WACCM-X, and PBMOD show relatively good association with R ranging from 0.76 to 0.82

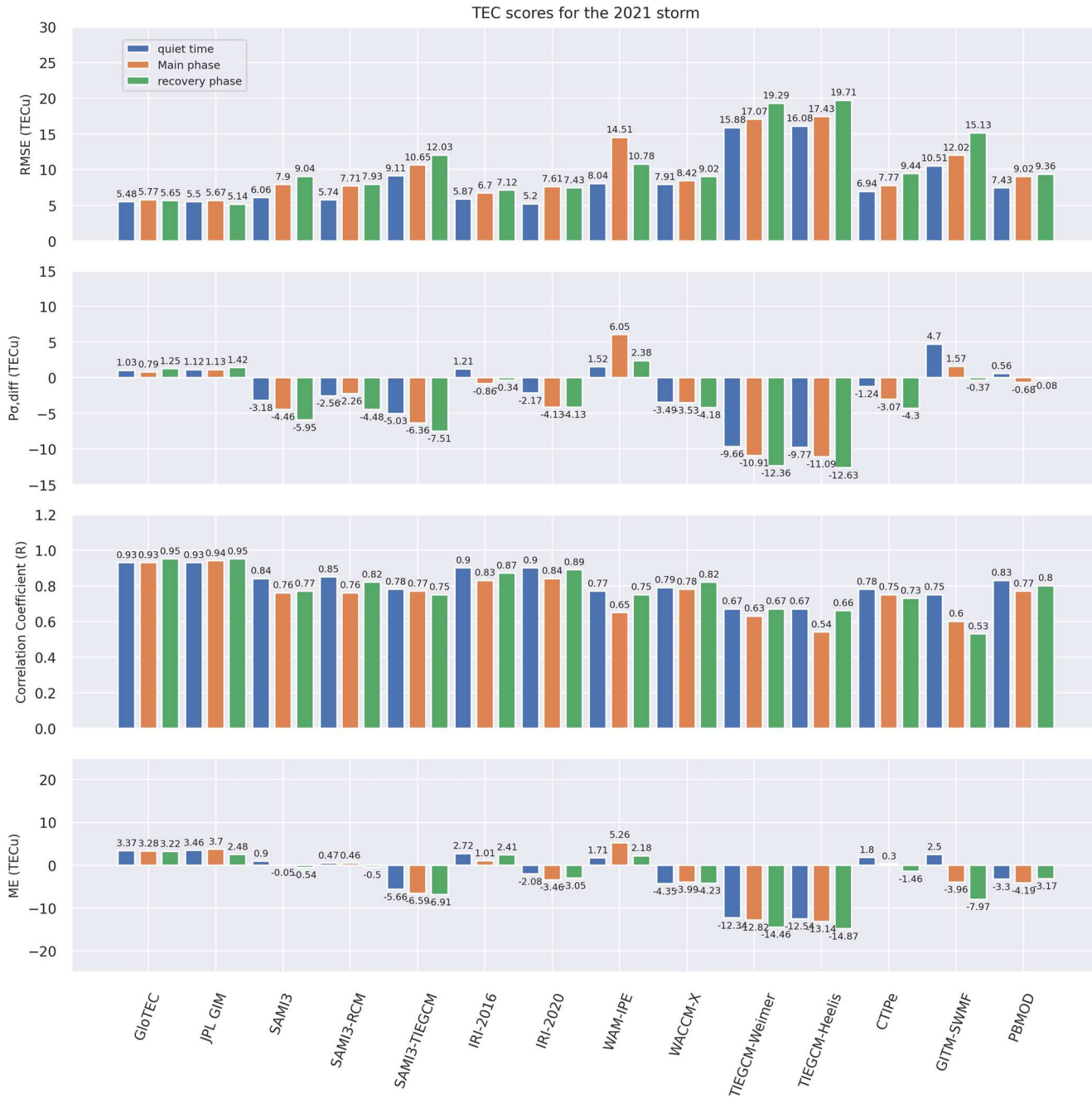

Figure 8. Same as Figure 3 but for the 2021 November storm.

during the main and recovery phases. TIEGCM-Heelis and GITM-SWMF have lower R of 0.54–0.66 and 0.53–0.6, respectively, during the main and recovery phases. During the quiet time, most models have R higher than 0.75, except TIEGCM-Weimer/Heelis. There appears a degradation of R for most of the empirical and physics-based models during the storm.

In the model bias category, it appears that GloTEC, JPL GIM, IRI-2016, and WAM-IPE systematically overestimate the TEC by about 1–5 TECu, and SAMI3, SAMI3-TIEGCM, IRI-2020, WACCM-X, TIEGCM-Weimer/Heelis, GITM-SWMF, and PBMOD systematically underestimate the TEC by about 2–15 TECu. We found that SAMI3-RCM has the smallest model bias within ±0.5 TECu. GloTEC and JPL GIM have model biases of about 2.5–3.7 TECu. SAMI3-TIEGCM, and TIEGCM-Weimer/Heelis have large model biases ranging from 7

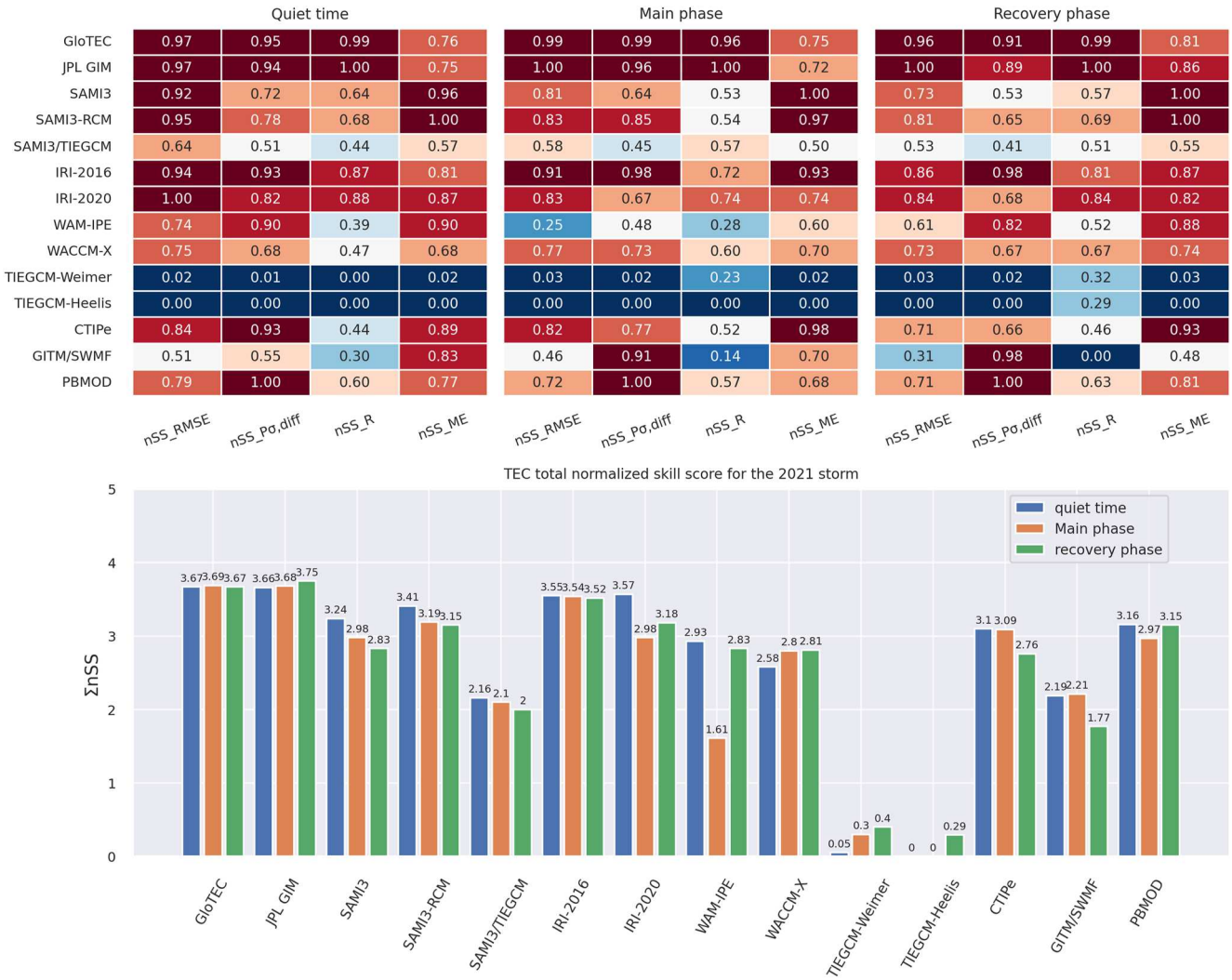

Figure 9. Same as Figure 4 but for the 2021 November storm.

to 15 TECu. Most models tend to have smaller bias during the solar minimum years, except TIEGCM-Weimer/Heelis, SAMI3-TIEGCM, and PBMOD.

In Figure 9, we calculate the normalized skill scores and total normalized skill scores for each model to compare the performance of ionospheric models against the reference model IRI-2016. The top panel shows the heat maps of normalized skill scores for each metric category and model during three phases. We further calculate the total normalized skill scores for comparison based on the summation of normalized skill scores ($\sum n$SS_metric). The total normalized skill scores (bottom panel) again reveal that GloTEC, JPL GIM, and IRI-2016 are the top three ionospheric models. For the physics-based model, SAMI3-RCM, CTIPe, PBMOD, and SAMI3 show good performance compared with other physics-based models.

We further examine the TEC change in response to the storm. Figure 10 shows the TC maps as a function of LT and MLAT during the main and recovery phases of the 2021 November storm. Madrigal TEC shows clear TEC variations up to ±50% during the main and recovery phases of the storm. It also shows a similar fork-shape distribution of TEC enhancements, but the 2021 November storm shows greater TEC variations than the 2013 March storm. The GloTEC and JPL GIM again show similar ionospheric variations and fork-shape patterns comparable with the Madrigal TEC. For the empirical models, IRI-2016 and 2020 generally show similar TEC variations of about ±15% during the storm times, implying that IRI models have relatively better performance during the solar minimum years. For the physics-based models, SAMI3-RCM, WAM-IPE, WACCM-X, and PBMOD show more

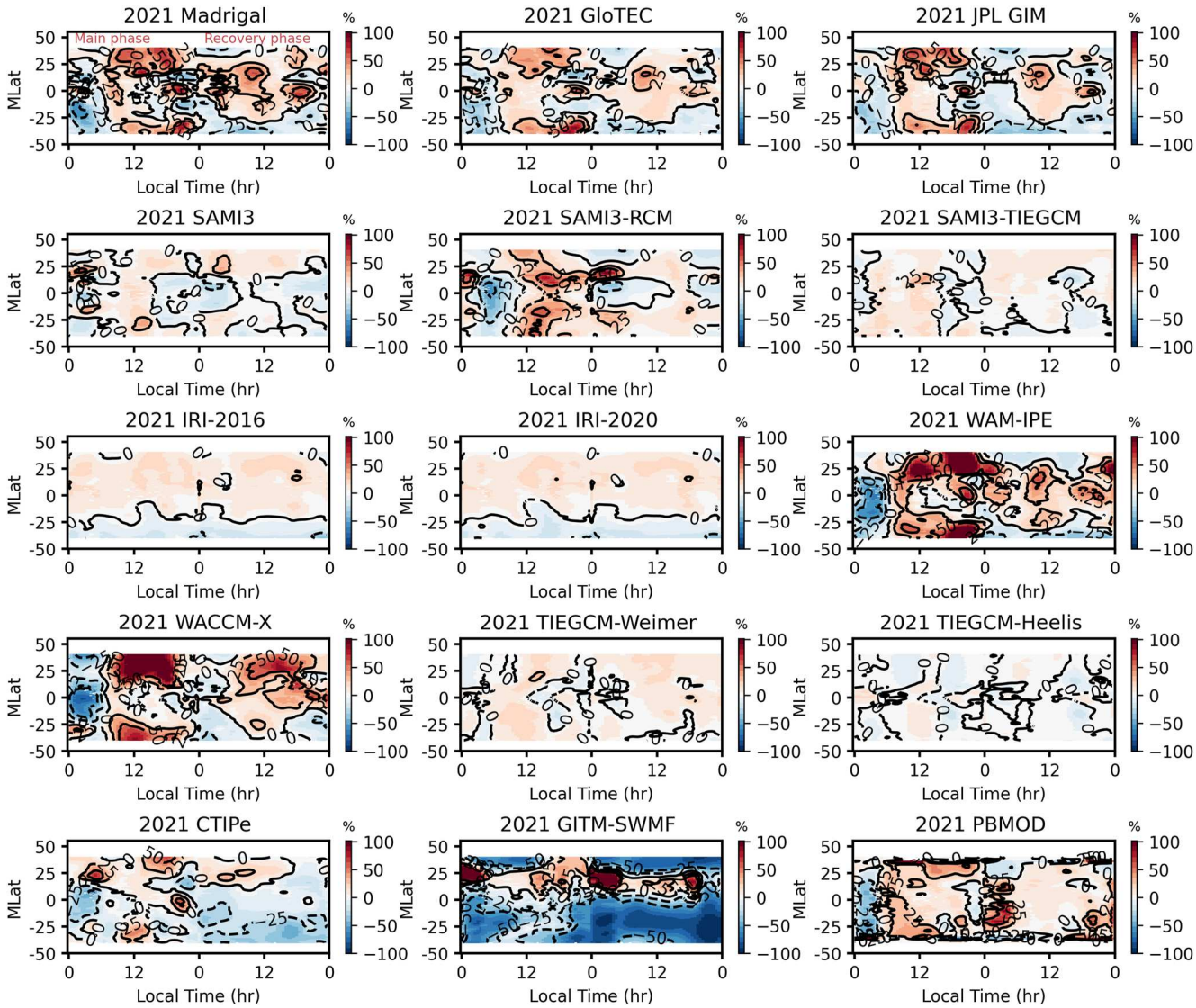

Figure 10. Same as Figure 5 but for the 2021 November storm.

significant TEC variations compared with other models, especially that WAM-IPE, WACCM-X, and PBMOD have error distributions comparable with Madrigal TEC, despite the amplitudes tend to be greater than Madrigal TEC.

Figure 11 is the same as Figure 6 but for the 2021 November storm. The top panel of Figure 11 shows the line plot and histogram, which denote the ratio of the TC difference at the 80th and 20th percentiles and the corresponding TC difference. The histogram shows that Madrigal TEC has TC of ~90% and ~60% during the main and recovery phases. The line plot and histogram show that WACCM-X has ratios close to 1 and TC of 86% and 55% during the main and recovery phases, demonstrating that WACCM-X well predicts the range of storm time TEC variations. Both GloTEC and JPL GIM have similar ratios of about 0.76 and 0.85 and TC values of ~68% and ~51% during the main and recovery phases. WAM-IPE and GITM-SWMF have greater TC of ~105% and 117% during the main phase, and ~69% and 68% during the recovery phase. On the other hand, other empirical and physics-based models have TC ratios close to 0 and TC changes smaller than 30%. TIEGCM-Heelis has TC close to 0%.

The line plot in the middle panel of Figure 11 shows the TC ratio at the 80th percentile between models and observation, and the histogram denotes the TC at the 80th percentile for each model. The line plot shows that WACCM-X has ratios of about 0.9 and 1.06 with positive TC of ~56% and 41% during the main and recovery phases, which is close to the Madrigal TEC that shows the storm mainly causes about 62% and 49% positive TC during the main and recovery phases. WAM-IPE has ratios close to 1.37 and 1.06, with a larger positive TC

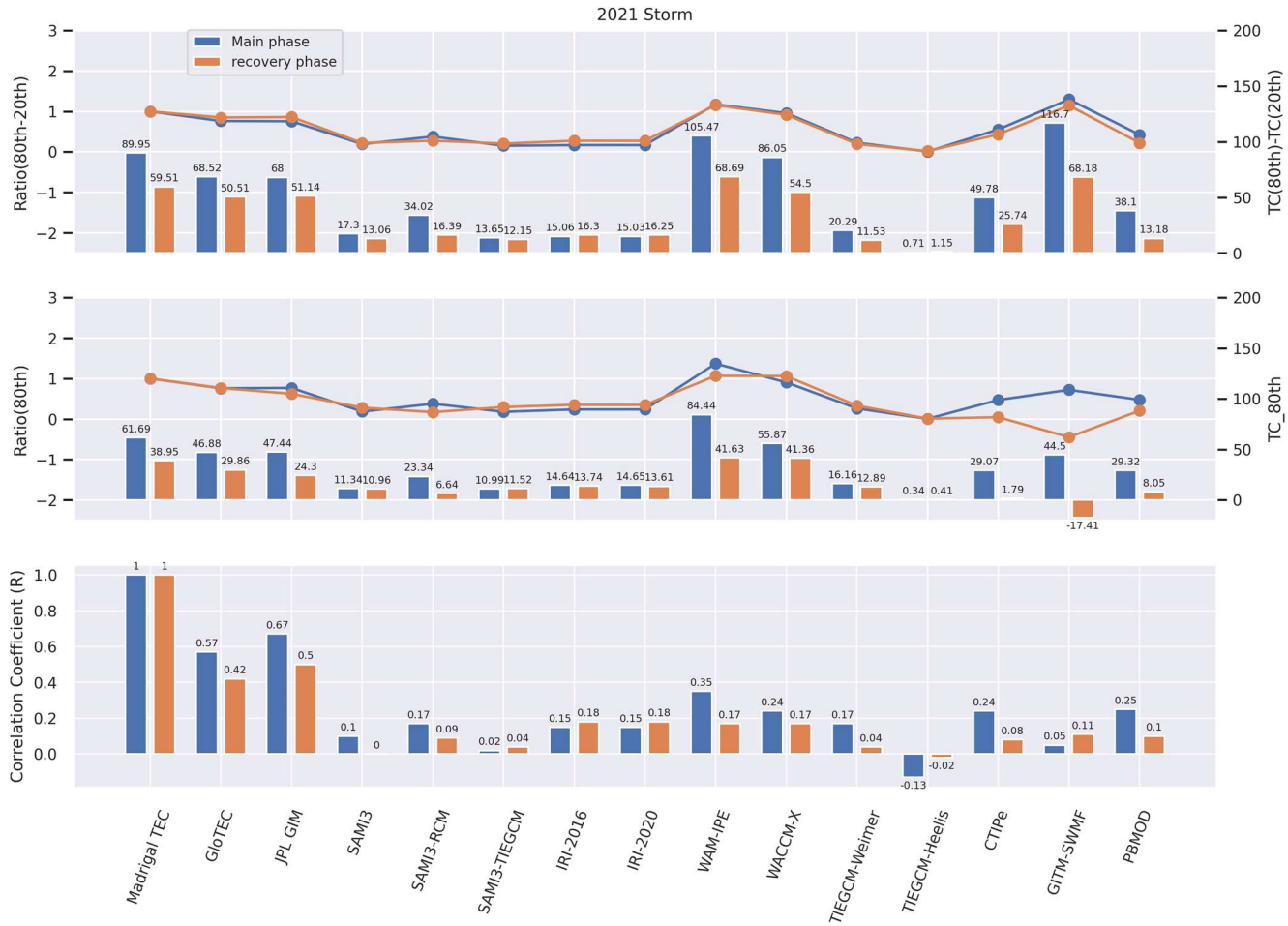

Figure 11. Same as Figure 6 but for the 2021 November storm.

of ~84% during the main phase and ~42% during the recovery phase. GloTEC has similar ratios of ~0.76 with positive TC of ~47% and 30% during the main and recovery phases, and JPL GIM has ratios of ~0.76 and 0.65 with positive TC of ~47% and 24% during the main and recovery phases.

The bottom panel of Figure 11 shows the correlation coefficient of TC. The GloTEC and JPL GIM, respectively, show higher correlation coefficients of 0.57 and 0.67 during the main phase, and 0.42 and 0.5 during the recovery phase. We find that all the physics-based and empirical models have low correlation coefficients since they cannot reflect the error distributions. WAM-IPE, WACCM-X, CTIPe, and PBMOD have relatively higher correlation coefficients of 0.35, 0.24, 0.24, and 0.25 during the main phase, and IRI-2016, IRI-2020, WAM-IPE, and WACCM-X have relatively higher correlation coefficients of 0.18, 0.18, 0.17, and 0.17 during the recovery phase.

Overall, GloTEC and JPL GIM show good performance in capturing the storm effect. WACCM-X and WAM-IPE can reasonably simulate the TEC relative changes during the storm times than other physics-based and empirical models. WAM-IPE shows a relatively higher correlation coefficient of 0.35 during the main phase, implying that WAM-IPE can well predict the spatial distribution of TEC changes.

5. Discussion and Conclusion

We have systematically and quantitatively evaluated and validated of ionospheric TEC derived from 14 ionospheric models hosted by NASA CCMC, NOAA SWPC, and NASA JPL to evaluate the capability of ionospheric models in simulating the storm time TEC. The modeled TEC has been compared with the Madrigal TEC during

the 2013 March and 2021 November storms. The validations include model-data comparison and assessment of models' capability in capturing TEC changes in response to storms.

For the model-data comparison, four fit performance metrics (RMSE, $P_{\sigma,\mathrm{diff}}$, R, ME) are used to evaluate the accuracy, precision, association, and bias of ionospheric models, and the normalized SS is proposed to understand the overall performance of the ionospheric models during the storm times. The total normalized SS suggests that GloTEC, JPL GIM, and IRI-2016 are the top three ionospheric models during the 2013 March and 2021 November storms. The DA or data-driven ionospheric models are expected to provide more accurate ionosphere TEC. Considering that GloTEC uses IRI-2016 as the background ionospheric model, the DA technique can efficiently improve the global ionospheric specification. For the physics-based model, we found that SAMI3-RCM, WACCM-X, and PBMOD have better performance during the 2013 March storm, and SAMI3-RCM, CTIPe, PBMOD, and SAMI3 show better performance during the 2021 November storm. This suggests that SAMI3-RCM and PBMOD may be the most stable physics-based models to predict the storm time TEC. We also note that most models have higher accuracy during the low solar flux year except TIEGCM-Wiemer/Heelis, and smaller bias except TIEGCM-Weimer/Heelis, SAMI3-TIEGCM, and PBMOD. Most physics-based models tend to underestimate the spread of TEC during the low solar flux year; however, WAM-IPE shows improvement in the low solar flux year.

We found that the fit performance metrics cannot well assess the models' capability in modeling the storm effect. For example, the empirical model IRI-2016 has higher metric scores than other physics-based models; however, it does not show significant storm effects. This is because the physics-based models tend to have systematical bias and often underestimate or overestimate the TEC when conducting model-data comparisons. To comprehensively evaluate the models' capability of capturing the storm anomaly, relative ionospheric quantity changes in response to storm should be considered.

For assessing the models' capability in capturing the storm time TEC anomaly, we calculate TC and estimate the ratios of TC between models and observation. GloTEC and JPL GIM again show the best performance in capturing the storm effect during the 2013 March and 2021 November storms. IRI-2016 and 2020 do not show clear storm effects, but they show minor improvements during the 2021 November storm. For the physics-based models, TIEGCM-Weimer and CTIPe show relatively good performance during the 2013 March storm; however, TIEGCM-Weimer degrades during the recovery phase. CTIPe shows a relatively higher correlation coefficient of 0.33 during the main and recovery phases, implying that CTIPe can reasonably predict the spatial and temporal distribution of TEC changes during the 2013 March storm. For the 2021 November storm, WACCM-X and WAM-IPE can better simulate the storm TEC anomaly. WACCM-X well captures the TEC changes, and WAM-IPE shows a relatively higher correlation coefficient of 0.35 during the main phase. Both WACCM-X and WAM-IPE reasonably capture the spatial and temporal distribution of TEC changes.

The physics-based models' performance during the moderate and low solar flux years is different. We found that the TIEGCM-Weimer/Heelis perform relatively well during the 2013 March storm; however, both models show significant degradation during the 2021 November storm. This implies that the neutral composition and temperature in TIEGCM may not be valid in solar minimum years. CTIPe can reasonably predict the TEC changes during the 2013 March storm, but it appears degradation during the 2021 November storm. WAM-IPE shows relatively good performance during the 2021 November storm, which may be due to the improvement of the lower atmospheric forcing using the 3DVar DA technique in the WAM state since the 2013 case is free run without DA. Further work is necessary to confirm the improvement of the DA technique by updating the WAM state for the WAM-IPE operational runs before 2021. WACCM-X generally performs better during the 2021 November storms, but the correlation coefficients are similar (0.17–0.23) during the 2021 and 2013 storms, suggesting that WACCM-X stably predicts the spatial and temporal distribution of TEC changes (Figures 5 and 10) in both low and moderate solar flux years. The implication is that the lower atmosphere forcing during storm times is still important for the global ionospheric specification.

Considering that the space environment can be influenced by the lower atmosphere (e.g., Liu, 2016), the difference between neutral atmospheric models used in the physics-based ionosphere models can significantly affect the ionosphere. SAMI3, SAMI3-RCM, and PBMOD use the empirical thermospheric models HWM and MSIS, which provide a general climatology of the neutral parameters, while WACCM-X, WAM-IPE, GITM-SWMF, and TIEGCM models self-consistently generate the neutral parameters. Meriwether et al. (2011) and Makela et al. (2013) have found disagreement between the HWM model and neutral wind observations. Huba and

Liu (2020) also found that the SAMI3 ionospheric simulations using the empirical thermospheric models cannot simulate plasma bubbles, suggesting that the lower atmospheric forcing and thermospheric winds play a vital role in the ionospheric electrodynamics. Furthermore, the comparison between SAMI3 simulations reveals that the inclusion of penetration electric fields from RCM improves the storm time global ionospheric specification (Huba, Sazykin, & Coster, 2017); however, storm time disturbance wind dynamo is not included (Fuller-Rowell et al., 1994; Maruyama et al., 2005). C. H. Lin et al. (2005) suggested that the enhanced wind fields and dynamo electric fields are essential in modifying the equatorial ionosphere. This suggests that the inclusion of more accurate neutral composition, temperature, and winds should be able to improve the global ionospheric simulations (e.g., Maute, 2017).

There are two important caveats to the present validation work. The first caveat is that GloTEC and JPL GIM are not independent of the Madrigal TEC. Thus, GloTEC and JPL GIM are expected to perform better than other models. Nevertheless, validations for GloTEC and JPL GIM are still necessary to evaluate the validity and capability of methodologies used to construct the global TEC maps (e.g., C. Y. Lin et al., 2017). The second caveat is that the validation only limits to the continents where the ground-based GNSS receivers are available. However, 70% of Earth's surface is covered by the oceans. The implication is that the performance of GloTEC and JPL GIM may degrade over the ocean regions due to the lack of observations. TEC validation, including the TEC observations observed by satellites or ocean-based instruments, is needed to comprehensively evaluate the models' performance (Azeem et al., 2020; Hsu et al., 2018).

Future validation works will include more ionospheric parameters, such as foF2, hmF2, electron density, plasma temperature, and ion drifts from satellite and ground-based instruments. These parameters are important for ionosphere validation since TEC could be partly affected by the upper boundary of ionosphere models. NASA CCMC also plans to have SAMI3-RCM and SAMI3-WACCM-X onboard for runs-on-request and improve the CCMC CAMEL validation tool (Rastätter et al., 2019) from 1-D time series to 2-D maps to support community model validation projects.

Data Availability Statement

The model outputs are available through the CCMC runs-on-request service (https://ccmc.gsfc.nasa.gov/tools/runs-on-request/) and simulation results (https://ccmc.gsfc.nasa.gov/ungrouped/IT/Iono_main.php). The Madrigal TEC is available from the Madrigal Database at Millstone Hill (http://cedar.openmadrigal.org/single?isGlobal=True&categories=17&instruments=8010). The NASA JPL GIM TEC is available at https://sideshow.jpl.nasa.gov/pub/iono_daily/gim_for_research/jpli/. The WAM-IPE outputs are available from the NOAA Space Weather Prediction Center (https://www.swpc.noaa.gov/products/wam-ipe) and CCMC (https://ccmc.gsfc.nasa.gov/external-runs/swpc/ionosphere/WAM-IPE/WAM-IPE-July2021-22/index.html). The Dst, Ap, and IMF Bz are available at Goddard Space Flight Center Space Physics Data Facility (https://omniweb.gsfc.nasa.gov/index.html).

Acknowledgments
This work was supported by NASA Goddard Space Flight Center through Cooperative Agreement 80NSSC21M0180 to Catholic University, Partnership for Heliophysics and Space Environment Research (PHaSER). Portions of the work were performed at the Jet Propulsion Laboratory, California Institute of Technology, under a contract with National Aeronautics and Space Administration (80NM0018D0004). Ja Soon Shim is supported by Korea Polar Research Institute (KOPRI) grant funded by the Ministry of Oceans and Fisheries (KOPRI PE23020) and basic research funding from the Korea Astronomy and Space Science Institute (KASI) (KASI2023185007). The work at Boston College was partially supported by NASA Grant 80HQTR20T0016.

References

Azeem, I., Crowley, G., Forsythe, V. V., Reynolds, A. S., Stromberg, E. M., Wilson, G. R., & Kohler, C. A. (2020). A new Frontier in ionospheric observations: GPS total electron content measurements from ocean buoys. *Space Weather*, *18*(11), e2020SW002571. https://doi.org/10.1029/2020SW002571

Basu, S., Basu, S., Valladares, C. E., Yeh, H. C., Su, S. Y., MacKenzie, E., et al. (2001). Ionospheric effects of major magnetic storms during the international space weather period of September and October 1999: GPS observations, VHF/UHF scintillations, and in situ density structures at middle and equatorial latitudes. *Journal of Geophysical Research*, *106*(A12), 30389–30413. https://doi.org/10.1029/2001JA001116

Bent, R. B., Llewellyn, S. K., Nesterczuk, G., & Schmid, P. E. (1975). The development of a highly successful world-wide empirical ionospheric model and its use in certain aspects of space communications and worldwide total electron content investigation. In J. M. Goodman (Ed.). *Proceedings of IES85* (pp. 23–38).

Bilitza, D. (2001). International reference ionosphere 2000. *Radio Science*, *36*(2), 261–275. https://doi.org/10.1029/2000rs002432

Bilitza, D., Altadill, D., Truhlik, V., Shubin, V., Galkin, I., Reinisch, B., & Huang, X. (2017). International Reference Ionosphere 2016: From ionospheric climate to real-time weather predictions. *Space Weather*, *15*(2), 418–429. https://doi.org/10.1002/2016SW001593

Bilitza, D., Pezzopane, M., Truhlik, V., Altadill, D., Reinisch, B. W., & Pignalberi, A. (2022). The International Reference Ionosphere model: A review and description of an ionospheric benchmark. *Reviews of Geophysics*, *60*(4), e2022RG000792. https://doi.org/10.1029/2022RG000792

Cai, Y., Yue, X., Wang, W., Zhang, S.-R., Liu, H., Lin, D., et al. (2022). Altitude extension of the NCAR-TIEGCM (TIEGCM-X) and evaluation. *Space Weather*, *20*(11), e2022SW003227. https://doi.org/10.1029/2022SW003227

Chartier, A. T., Datta-Barua, S., McDonald, S. E., Bust, G. S., Tate, J., Goncharenko, L. P., et al. (2021). Night-time ionospheric localized enhancements (NILE) observed in North America following geomagnetic disturbances. *Journal of Geophysical Research: Space Physics*, *126*(9), e2021JA029324. https://doi.org/10.1029/2021JA029324

Chen, C. H., Lin, C. H., Chang, L. C., Huba, J. D., Lin, J. T., Saito, A., & Liu, J. Y. (2013). Thermospheric tidal effects on the ionospheric midlatitude summer nighttime anomaly using SAMI3 and TIEGCM. *Journal of Geophysical Research: Space Physics*, *118*(6), 3836–3845. https://doi.org/10.1002/jgra.50340

Chen, C. H., Lin, C. H., Matsuo, T., Chen, W. H., Lee, I. T., Liu, J. Y., et al. (2016). Ionospheric data assimilation with thermosphere-ionosphere-electrodynamics general circulation model and GPS-TEC during geomagnetic storm conditions. *Journal of Geophysical Research: Space Physics*, *121*(6), 5708–5722. https://doi.org/10.1002/2015JA021787

Codrescu, M. V., Negrea, C., Fedrizzi, M., Fuller-Rowell, T. J., Dobin, A., Jakowsky, N., et al. (2012). A real-time run of the coupled thermosphere ionosphere plasmasphere electrodynamics (CTIPe) model. *Space Weather*, *10*(2), S02001. https://doi.org/10.1029/2011SW000736

Drob, D. P., Emmert, J. T., Crowley, G., Picone, J. M., Shepherd, G. G., Skinner, W., et al. (2008). An empirical model of the Earth's horizontal wind fields: HWM07. *Journal of Geophysical Research*, *113*(A12), A12304. https://doi.org/10.1029/2008JA013668

Fang, T.-W., Kubaryk, A., Goldstein, D., Li, Z., Fuller-Rowell, T., Millward, G., et al. (2022). Space weather environment during the SpaceX Starlink satellite loss in February 2022. *Space Weather*, *20*(11), e2022SW003193. https://doi.org/10.1029/2022SW003193

Fejer, B. G., Jensen, J. W., & Su, S.-Y. (2008). Quiet time equatorial F region vertical plasma drift model derived from ROCSAT-1 observations. *Journal of Geophysical Research*, *113*(A5), A05304. https://doi.org/10.1029/2007JA012801

Fuller-Rowell, T. J., Akmaev, R. A., Wu, F., Anghel, A., Maruyama, N., Anderson, D. N., et al. (2008). Impact of terrestrial weather on the upper atmosphere. *Geophysical Research Letters*, *35*(9), L09808. https://doi.org/10.1029/2007GL032911

Fuller-Rowell, T. J., Codrescu, M. C., & Wilkinson, P. (2000). Quantitative modeling of the ionospheric response to geomagnetic activity. *Annales de Geophysique*, *18*(7), 766–781. https://doi.org/10.1007/s00585-000-0766-7

Fuller-Rowell, T. J., Codrescu, M. V., Moffet, R. J., & Quegan, S. (1994). Response of the thermosphere and ionosphere to geomagnetic storms. *Journal of Geophysical Research*, *99*(A3), 3893–3914. https://doi.org/10.1029/93ja02015

Fuller-Rowell, T. J., & Evans, D. S. (1987). Height-integrated Pedersen and Hall conductivity patterns inferred from the TIROS-NOAA satellite data. *Journal of Geophysical Research*, *92*(A7), 7606–7618. https://doi.org/10.1029/ja092ia07p07606

Fuller-Rowell, T. J., & Rees, D. (1980). A three-dimensional time-dependent global model of the thermosphere. *Journal of the Atmospheric Sciences*, *37*(11), 2545–2567. https://doi.org/10.1175/1520-0469(1980)037<2545:ATDTDG>2.0.CO;2

Goncharenko, L. P., Tamburri, C. A., Tobiska, W. K., Schonfeld, S. J., Chamberlin, P. C., Woods, T. N., et al. (2021). A new model for ionospheric total electron content: The impact of solar flux proxies and indices. *Journal of Geophysical Research: Space Physics*, *126*(2), e2020JA028466. https://doi.org/10.1029/2020JA028466

Hedin, A. E. (1991). Extension of the MSIS thermosphere model into the middle and lower atmosphere. *Journal of Geophysical Research*, *96*(A2), 1159–1172. https://doi.org/10.1029/90JA02125

Heelis, R. A., Lowell, J. K., & Spiro, R. W. (1982). A model of the high-latitude ionospheric convection pattern. *Journal of Geophysical Research*, *87*(A8), 6339–6345. https://doi.org/10.1029/JA087iA08p06339

Hsu, C.-T., Matsuo, T., & Liu, J.-Y. (2018). Impact of assimilating the FORMOSAT-3/COSMIC and FORMOSAT-7/COSMIC-2 RO data on the midlatitude and low-latitude ionospheric specification. *Earth and Space Science*, *5*(12), 875–890. https://doi.org/10.1029/2018EA000447

Huba, J. D., Joyce, G., Sazykin, S., Wolf, R., & Spiro, R. (2005). Simulation study of penetration electric field effects on the low- to mid-latitude ionosphere. *Geophysical Research Letters*, *32*(23), L23101. https://doi.org/10.1029/2005GL024162

Huba, J. D., & Liu, H.-L. (2020). Global modeling of equatorial spread F with SAMI3/WACCM-X. *Geophysical Research Letters*, *47*(14), e2020GL088258. https://doi.org/10.1029/2020GL088258

Huba, J. D., Maute, A., & Crowley, G. (2017). SAMI3_ICON: Model of the ionosphere/plasmasphere system. *Space Science Reviews*, *212*(1–2), 731–742. https://doi.org/10.1007/s11214-017-0415-z

Huba, J. D., & Sazykin, S. (2014). Storm time ionosphere and plasmasphere structuring: SAMI3-RCM simulation of the 31 March 2001 geomagnetic storm. *Geophysical Research Letters*, *41*(23), 8208–8214. https://doi.org/10.1002/2014GL062110

Huba, J. D., Sazykin, S., & Coster, A. (2017). SAMI3-RCM simulation of the 17 March 2015 geomagnetic storm. *Journal of Geophysical Research: Space Physics*, *122*(1), 1246–1257. https://doi.org/10.1002/2016JA023341

Hurrell, J. W., Holland, M. M., Gent, P. R., Ghan, S., Kay, J. E., Kushner, P. J., et al. (2013). The community Earth system model: A framework for collaborative research. *Bulletin of the American Meteorological Society*, *94*(9), 1339–1360. https://doi.org/10.1175/BAMS-D-12-00121.1

Kataoka, R., Shiota, D., Fujiwara, H., Jin, H., Tao, C., Shinagawa, H., & Miyoshi, Y. (2022). Unexpected space weather causing the reentry of 38 Starlink satellites in February 2022. *Journal of Space Weather and Space Climate*, *12*, 41. https://doi.org/10.1051/swsc/2022034

Kelley, M. C., Fejer, B. G., & Gonzales, C. A. (1979). An explanation for anomalous equatorial ionospheric electric fields associated with a northward turning of the interplanetary magnetic field. *Geophysical Research Letters*, *6*(4), 301–304. https://doi.org/10.1029/GL006i004p00301

Kelley, M. C., Makela, J. J., Chau, J. L., & Nicolls, M. J. (2003). Penetration of the solar wind electric field into the magnetosphere/ionosphere system. *Geophysical Research Letters*, *30*(4), 1158. https://doi.org/10.1029/2002GL016321

Liemohn, M. W., Shane, A. D., Azari, A. R., Petersen, A. K., Swiger, B. M., & Mukhopadhyay, A. (2021). RMSE is not enough: Guidelines to robust data-model comparisons for magnetospheric physics. *Journal of Atmospheric and Solar-Terrestrial Physics*, *218*, 105624. https://doi.org/10.1016/j.jastp.2021.105624

Lin, C. H., Richmond, A. D., Heelis, R. A., Bailey, G. J., Lu, G., Liu, J. Y., et al. (2005). Theoretical study of the low- and midlatitude ionospheric electron density enhancement during the October 2003 superstorm: Relative importance of the neutral wind and the electric field. *Journal of Geophysical Research*, *110*(A12), A12312. https://doi.org/10.1029/2005JA011304

Lin, C.-Y., Lin, C. C.-H., Liu, J.-Y., Rajesh, P. K., Matsuo, T., Chou, M.-Y., et al. (2020). The early results and validation of FORMOSAT-7/COSMIC-2 space weather products: Global ionospheric specification and Ne-aided Abel electron density profile. *Journal of Geophysical Research: Space Physics*, *125*(10), e2020JA028028. https://doi.org/10.1029/2020JA028028

Lin, C. Y., Matsuo, T., Liu, J. Y., Lin, C. H., Huba, J. D., Tsai, H. F., & Chen, C. Y. (2017). Data assimilation of ground-based GPS and radio occultation total electron content for global ionospheric specification. *Journal of Geophysical Research: Space Physics*, *122*(10), 10876–10886. https://doi.org/10.1002/2017JA024185

Lin, D., Wang, W., Garcia-Sage, K., Yue, J., Merkin, V., McInerney, J. M., et al. (2022). Thermospheric neutral density variation during the "SpaceX" storm: Implications from physics-based whole geospace modeling. *Space Weather*, *20*(12), e2022SW003254. https://doi.org/10.1029/2022SW003254

Liu, H.-L. (2016). Variability and predictability of the space environment as related to lower atmosphere forcing. *Space Weather*, *14*, 634–658. https://doi.org/10.1002/2016SW001450

Liu, H.-L., Bardeen, C. G., Foster, B. T., Lauritzen, P., Liu, J., Lu, G., et al. (2018). Development and validation of the whole atmosphere community climate model with thermosphere and ionosphere extension (WACCM-X 2.0). *Journal of Advances in Modeling Earth Systems*, *10*(2), 381–402. https://doi.org/10.1002/2017MS001232

Liu, L., Morton, Y. J., & Liu, Y. (2022). ML prediction of global ionospheric TEC maps. *Space Weather*, *20*(9), e2022SW003135. https://doi.org/10.1029/2022SW003135

Llewellyn, S. K., & Bent, R. B. (1973). *Documentation and description of the Bent ionospheric model*. Rep AFCRL-TR-73-0657. Air Force Geophys. Lab., Hanscom Air Force Base.

Makela, J. J., Fisher, D. J., Meriwether, J. W., Buriti, R. A., & Medeiros, A. F. (2013). Near-continual ground-based nighttime observations of thermospheric neutral winds and temperatures over equatorial Brazil from 2009 to 2012. *Journal of Atmospheric and Solar-Terrestrial Physics*, *103*, 94–102. https://doi.org/10.1016/j.jastp.2012.11.019

Mannucci, A. J., Iijima, B., Sparks, L., Pi, X. Q., Wilson, B., & Lindqwister, U. (1999). Assessment of global TEC mapping using a three-dimensional electron density model. *Journal of Atmospheric and Solar-Terrestrial Physics*, *61*(16), 1227–1236. https://doi.org/10.1016/S1364-6826(99)00053-X

Mannucci, A. J., Wilson, B. D., Yuan, D. N., Ho, C. H., Lindqwister, U. J., & Runge, T. F. (1998). A global mapping technique for GPS-derived ionospheric total electron content measurements. *Radio Science*, *33*(3), 565–582. https://doi.org/10.1029/97RS02707

Maruyama, N., Richmond, A. D., Fuller-Rowell, T. J., Codrescu, M. V., Sazykin, S., Toffoletto, F. R., et al. (2005). Interaction between direct penetration and disturbance dynamo electric fields in the storm-time equatorial ionosphere. *Geophysical Research Letters*, *32*(17), L17105. https://doi.org/10.1029/2005GL023763

Maruyama, N., Sun, Y.-Y., Richards, P. G., Middlecoff, J., Fang, T.-W., Fuller-Rowell, T. J., et al. (2016). A new source of the midlatitude ionospheric peak density structure revealed by a new Ionosphere-Plasmasphere model. *Geophysical Research Letters*, *43*(6), 2429–2435. https://doi.org/10.1002/2015GL067312

Maute, A. (2017). Thermosphere-ionosphere-electrodynamics general circulation model for the ionospheric connection explorer: TIEGCM-ICON. *Space Science Reviews*, *212*(1–2)), 523–551. https://doi.org/10.1007/s11214-017-0330-3

McDonald, S. E., Sassi, F., & Mannucci, A. J. (2015). SAMI3/SD-WACCM-X simulations of ionospheric variability during northern winter 2009. *Space Weather*, *13*(9), 568–584. https://doi.org/10.1002/2015SW001223

Meriwether, J., Makela, J., Huang, Y., Fisher, D., Buriti, R., Medeiros, A., & Takahashi, H. (2011). Climatology of the nighttime equatorial thermospheric winds and temperatures over Brazil near solar minimum. *Journal of Geophysical Research*, *116*(A4), A04322. https://doi.org/10.1029/2011JA016477

Perlongo, N. J., Ridley, A. J., Cnossen, I., & Wu, C. (2018). A year-long comparison of GPS TEC and global ionosphere-thermosphere models. *Journal of Geophysical Research: Space Physics*, *123*(2), 1410–1428. https://doi.org/10.1002/2017JA024411

Rajesh, P. K., Lin, C. H., Lin, C. Y., Chen, C. H., Liu, J. Y., Matsuo, T., et al. (2021). Extreme positive ionosphere storm triggered by a minor magnetic storm in deep solar minimum revealed by FORMOSAT-7/COSMIC-2 and GNSS observations. *Journal of Geophysical Research: Space Physics*, *126*(2), e2020JA028261. https://doi.org/10.1029/2020JA028261

Rastätter, L., Shim, J. S., Kuznetsova, M. M., Kilcommons, L. M., Knipp, D. J., Codrescu, M., et al. (2016). GEM-CEDAR challenge: Poynting flux at DMSP and modeled Joule heat. *Space Weather*, *14*(2), 113–135. https://doi.org/10.1002/2015SW001238

Rastätter, L., Wiegand, C., Mullinix, R. E., & MacNeice, P. J. (2019). Comprehensive assessment of models and events using library tools (CAMEL) framework: Time series comparisons. *Space Weather*, *17*(6), 845–860. https://doi.org/10.1029/2018SW002043

Retterer, J. M. (2005). Physics-based forecasts of equatorial radio scintillation for the communication and navigation outage forecasting system (C/NOFS). *Space Weather*, *3*(12), S12C03. https://doi.org/10.1029/2005SW000146

Richmond, A. D., Ridley, E. C., & Roble, R. G. (1992). A thermosphere/ionosphere general circulation model with coupled electrodynamics. *Geophysical Research Letters*, *19*(6), 601–604. https://doi.org/10.1029/92gl00401

Ridley, A. J., Deng, Y., & Tóth, G. (2006). The global ionosphere-thermosphere model. *Journal of Atmospheric and Solar-Terrestrial Physics*, *68*(8), 839–864. https://doi.org/10.1016/j.jastp.2006.01.008

Ringuette, R., De Zeeuw, D., Rastaetter, L., Pembroke, A., Gerland, O., & Garcia-Sage, K. (2022). Kamodo's modelagnostic satellite flythrough: Lowering the utilization barrier for heliophysics model outputs. *Frontiers in Astronomy and Space Sciences*, *9*, 1005977. https://doi.org/10.3389/fspas.2022.1005977

Roble, R. G., & Ridley, E. C. (1987). An auroral model for the NCAR thermosphere general circulation model (TGCM). *Annales Geophysicae - Series A: Upper Atmosphere and Space Sciences*, *5*(6), 369–382.

Scherliess, L., & Fejer, B. G. (1999). Radar and satellite global equatorial F region vertical drift model. *Journal of Geophysical Research*, *104*(A4), 6829–6842. https://doi.org/10.1029/1999JA900025

Scherliess, L., Schunk, R. W., Sojka, J. J., Thompson, D. C., & Zhu, L. (2006). Utah State University global assimilation of ionospheric measurements Gauss-Markov Kalman filter model of the ionosphere: Model description and validation. *Journal of Geophysical Research*, *111*(A11), A11315. https://doi.org/10.1029/2006JA011712

Scherliess, L., Tsagouri, I., Yizengaw, E., Bruinsma, S., Shim, J. S., Coster, A., & Retterer, J. M. (2019). The International Community Coordinated Modeling Center space weather modeling capabilities assessment: Overview of ionosphere/thermosphere activities. *Space Weather*, *17*(4), 527–538. https://doi.org/10.1029/2018SW002036

Schunk, R. W., Scherliess, L., & Sojka, J. J. (2002). Ionospheric specification and forecast modeling. *Journal of Spacecraft and Rockets*, *39*(2), 314–324. https://doi.org/10.2514/2.3815

Schunk, R. W., Scherliess, L., Sojka, J. J., Thompson, D. C., Anderson, D. N., Codrescu, M., et al. (2004). Global assimilation of ionospheric measurements (GAIM). *Radio Science*, *39*(1), RS1S02. https://doi.org/10.1029/2002RS002794

Shim, J. S., Kuznetsova, M., Rastätter, L., Bilitza, D., Butala, M., Codrescu, M., et al. (2012). CEDAR Electrodynamics Thermosphere Ionosphere (ETI) Challenge for systematic assessment of ionosphere/thermosphere models: Electron density, neutral density, NmF2, and hmF2 using space based observations. *Space Weather*, *10*, S10004. https://doi.org/10.1029/2012SW000851

Shim, J. S., Kuznetsova, M., Rastätter, L., Hesse, M., Bilitza, D., Butala, M., et al. (2011). CEDAR electrodynamics thermosphere ionosphere (ETI) challenge for systematic assessment of ionosphere/thermosphere models: NmF2, hmF2, and vertical drift using ground-based observations. *Space Weather*, *9*(12), S12003. https://doi.org/10.1029/2011SW000727

Shim, J. S., Tsagouri, I., Goncharenko, L., Rastaetter, L., Kuznetsova, M., Bilitza, D., et al. (2018). Validation of ionospheric specifications during geomagnetic storms: TEC and foF2 during the 2013 March storm event. *Space Weather*, *16*(11), 1686–1701. https://doi.org/10.1029/2018SW002034

Shultz, D. (2014). 'Space bubbles' may have led to deadly battle in Afghanistan. *Science*. https://doi.org/10.1126/article.22392

Sun, Y. Y., Liu, J. Y., Tsai, H. F., & Krankowski, A. (2017). Global ionosphere map constructed by using total electron content from ground-based GNSS receiver and FORMOSAT-3/COSMIC GPS occultation experiment. *GPS Solutions*, *21*(4), 1583–1591. https://doi.org/10.1007/s10291-017-0635-4

Titheridge, J. E. (1997). Model results for the ionospheric E region: Solar and seasonal changes. *Annales Geophysicae*, *15*(1), 63–78. https://doi.org/10.1007/s00585-997-0063-9

Tóth, G., Sokolov, I. V., Gombosi, T. I., Chesney, D. R., Clauer, C. R., De Zeeuw, D. L., et al. (2005). Space Weather Modeling Framework A new tool for the space science community. *Journal of Geophysical Research*, *110*(A12), A12226. https://doi.org/10.1029/2005JA011126

Tóth, G., Van der Holst, B., Sokolov, I. V., De Zeeuw, D. L., Gombosi, T. I., Fang, F., et al. (2012). Adaptive numerical algorithms in space weather modeling. *Journal of Computational Physics*, *231*(3), 870–903. https://doi.org/10.1016/j.jcp.2011.02.006

Wang, Z., Zou, S., Coppeans, T., Ren, J., Ridley, A., & Gombosi, T. (2019). Segmentation of SED by boundary flows associated with westward drifting partial ring current. *Geophysical Research Letters*, *46*(14), 7920–7928. https://doi.org/10.1029/2019GL084041

Weimer, D. R. (2005). Improved ionospheric electrodynamic models and application to calculating Joule heating rates. *Journal of Geophysical Research*, *110*(A5), A05306. https://doi.org/10.1029/2004JA010884